





39 **Plain Language Summary**

40 Fluvial terraces and alluvial fans in the Toro Basin, NW Argentina record river evolution and global  
41 climate cycles over time. Landform dating reveals lower-frequency climate cycles (100-kyr) preserved  
42 downstream and higher-frequency cycles (21/40-kyr) upstream, supporting theoretical predications that  
43 longer rivers filter out higher-frequency climate signals. This finding improves our understanding of  
44 the spatial distribution of sedimentary paleoclimate records within landscapes.

45

46

47 **1. Introduction**

48

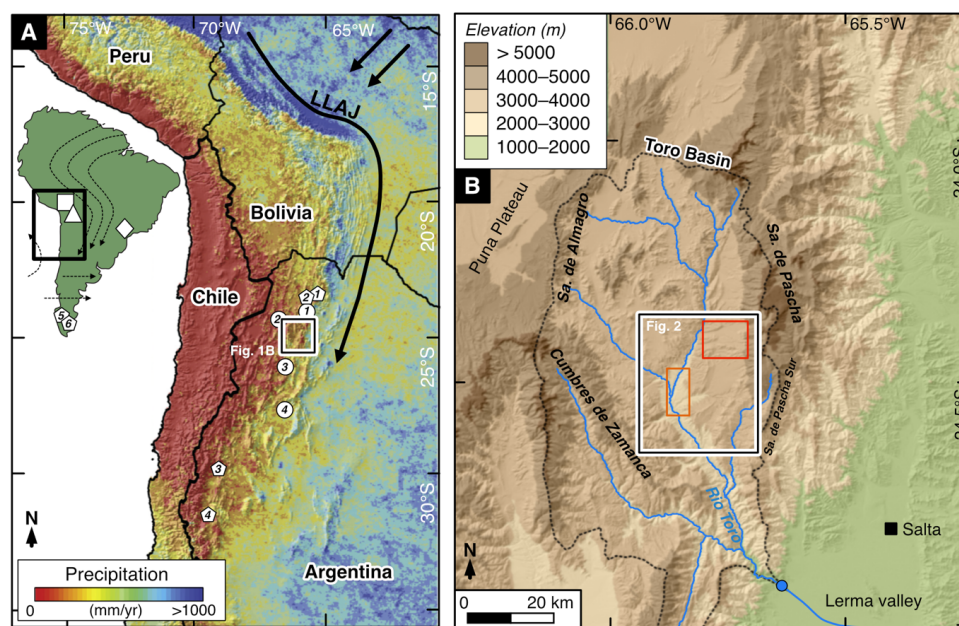
49 Fluvial landforms, sediment deposits and the channel form of alluvial systems can be used to reveal  
50 landscape response to past environmental change (Castelltort and Van Den Driessche, 2003, Godard et  
51 al., 2013; Dey et al., 2016; Romans et al., 2016; Mescolotti et al., 2021). Alluvial channels respond to  
52 climate or tectonic driven changes in water discharge, sediment discharge, or base level elevation by  
53 adjusting at least one of their characteristics: bed slope, channel width, channel depth, sediment  
54 transport rates or grain-size distribution (Mackin 1948; Savi et al., 2020). We can observe this channel  
55 adjustment via sediment aggradation or incision events, which modify channel bed elevations (Howard,  
56 1982; van den Berg et al., 2008; Wickert and Schildgen, 2019; Tofelde et al., 2019). Fluvial landforms  
57 such as terraces and alluvial fans, which develop along these channels because of this aggradation or  
58 incision, can provide a useful record of how the alluvial-channel system has evolved over time (Rohais  
59 et al., 2012; Armitage et al., 2013; Kober et al., 2013; Counts et al., 2015; Mather et al., 2017; Tofelde  
60 et al., 2021).

61

62 Theory suggests that the time required for an alluvial-channel long profile to adjust to a change in  
63 climate forcing (response time) varies with the magnitude and type of the forcing (sediment supply  
64 versus water supply) and the length of the system; shorter systems respond faster and, hence, may record  
65 a higher frequency of forcing compared to longer systems (Paola et al., 1992; Castelltort and Van Den  
66 Driessche, 2003; Godard et al., 2013; McNab et al., 2023). The length scale over which periodic forcing  
67 delivered at the channel head affects the channel long profile is proportional to the square root of the  
68 period of the forcing (Paola et al., 1992), which means that higher frequency forcing is filtered out with  
69 distance downstream. Evidence of this relationship is preserved in several sedimentary basins in the  
70 Central Andes. Tributary catchments of the Humahuaca Basin (23°S) retain late Quaternary fluvial  
71 deposits between 10 and 100 km downstream from the basin headwaters, which record precessional (21  
72 kyr) cycles in aggradation and incision (Schildgen et al., 2016). In the Toro Basin (24.5°S), a flight of  
73 fluvial cut-and-fill terraces with periodicity of 100-kyr has been linked to eccentricity-driven climate  
74 change (Tofelde et al., 2017). These terraces have an upstream channel length of ~60–80 km. Pliocene-



75 Late Pleistocene sediment deposits are preserved ~140–160 km downstream from the headwaters of  
 76 the Iruya Basin (22°S) of the northern Central Andes and record long eccentricity (400-kyr) cycles  
 77 (Fisher et al., 2023). Crucially, only a single climate periodicity has been recorded in each these basins  
 78 to date. To further test this theoretical relationship between climate periodicity and system length, we  
 79 aim to investigate whether multiple periodicities can be preserved within a single basin, and if this is  
 80 the case, whether higher frequency climate forcing is only observed in the uppermost reaches of the  
 81 basin.  
 82



83  
 84 **Figure 1.** Overview of the topography, rainfall and moisture transport of the Central Andes. A) TRMM2B31 rainfall map  
 85 (Bookhagen and Strecker, 2008). Moisture is transported (black arrows) from Atlantic sources during the SASM by the Low-  
 86 Level Andean Jet (LLAJ; Vera et al., 2006). The Toro Basin is outlined by the white-black bordered box. Circle symbols  
 87 denote regional glacial record locations: (1) Nevado de Chañi (24.0°S, 65.7°W; Martini et al., 2017), (2) Quevar Volcano  
 88 (24.4°S, 66.8°W; Luna et al., 2018), (3) Sierra de Quilmes (26.2°S, 66.2°W; Zech et al., 2017) and the (4) Sierra de Aconquija  
 89 (27.2°S, 66.1°W; D’Arcy et al., 2019a). Pentagon symbols denote MPT geomorphic record locations: (1) Casa Grande Basin  
 90 (23°S, 66.5°W; Pingel et al., 2019b), (2) Salinas Grandes Basin (23.5°S, 66°W; Pingel et al., 2019b), (3) Iglesia Basin (30.5°S,  
 91 69°W; Terrizzano et al., 2017), (4) Calingasta Basin (32°S, 69.5°W; Peri et al., 2022), (5) Río Deseado (47°S, 72°W; Tobal et  
 92 al., 2021), (6) Río Santa Cruz (50°S, 73°W; Milanez Fernandes, 2023). Inset map of South America indicates Fig. 1A extent  
 93 and the location of the Lake Titicaca (square symbol; Fritz et al., 2007), Salar de Uyuni (triangle symbol; Baker et al., 2001)  
 94 and Botuverá Cave (diamond symbol; Wang et al., 2007) paleoenvironmental records. Dashed arrows outline the moisture-  
 95 bearing low-level airflow patterns for South America which are deflected by the Andean topography. B) Topography of the  
 96 Toro Basin (ca. 4000 km<sup>2</sup>, 1500-5900 m asl) from TanDEM-X (12-m resolution) elevation data. Basin outlined by dashed  
 97 black line. Upper basin delineated by white-black bordered rectangle (see Fig. 2). Toro alluvial fans and fluvial terraces  
 98 outlined by red and orange rectangles, respectively. Basin outlet and start of long profile in Fig. 2 is shown by blue circle. Sa.  
 99 – Sierra.

100  
 101 Approximately 30 km upstream of the 100-kyr cut-and fill terraces in the Toro Basin is a suite of well-  
 102 preserved alluvial fan surfaces which extend from tributary catchments that drain the Sierra de Pascha  
 103 (Fig. 1). There is limited evidence of sediment storage in these tributary catchments en route to the fans.  
 104 With an upstream channel length of ~10 km, this fan record may capture geomorphic change linked to



105 a higher frequency climate forcing than the downstream terraces. The Toro Basin alluvial-channel  
106 system therefore allows us to explore (1) how channel responses to external perturbations may or may  
107 not propagate downstream, and (2) the differences in landscape response to forcing frequency as a  
108 function of channel length when comparing the upper basin alluvial fan deposits with the lower basin  
109 terrace sequence.

110

111 To address these aims, we dated the suite of fan surfaces in the upper Toro Basin using *in situ*-<sup>10</sup>Be  
112 cosmogenic radionuclide (CRN) dating. We used our new Toro fan chronostratigraphy in conjunction  
113 with the fluvial terrace record of Tofelde et al. (2017) to further characterise the evolution of the Toro  
114 Basin over the last million years.

115

## 116 **2. Regional setting**

117

118 The Toro Basin (24.5°S) is an intermontane basin in the Eastern Cordillera of NW Argentina, located  
119 between the high elevation Puna Plateau to the west and the low elevation Andean foreland to the east  
120 (Fig. 1). The mainly gravel-bedded Río Toro flows predominantly south from the low relief upper  
121 reaches of the basin with thick successions of preserved sediment, which are the focus of this study  
122 (referred to as the upper Toro Basin herein), through a steep bedrock gorge, before draining into the  
123 Cabra Corral reservoir in the Lerma valley (Marrett and Strecker 2000; DeCelles et al., 2011). The  
124 diffuse shifts in channel steepness along its course are characteristic of arid, tectonically active  
125 landscapes with mechanically strong basement rocks (Fig. 2B, C) (Bernard et al., 2019, Zondervan et  
126 al., 2020; Seagren and Schoenbohm, 2021).

127

### 128 **2.1 Geology and tectonic setting**

129 The upper Toro Basin is confined by three reverse-fault bounded basement ranges: 1) the Cumbres de  
130 Zamaca bounded by the west-dipping Solá Fault in the west, 2) the Sierra de Almagro bounded by the  
131 northwest-dipping San Bernardo fault in the north, and 3) the Sierra de Pascha Ranges and the east-  
132 dipping Gólgota Fault in the east (Marrett and Strecker 2000) (Fig. 1, 2). The Solá fault has been active  
133 since at least the Pliocene, and tectonic deformation from the Miocene to mid-Pleistocene has been  
134 recorded along the San Bernardo and Gólgota faults (Marrett and Strecker 2000). The Gólgota fault  
135 reactivated after ca. 0.98 Ma (Hilley and Strecker 2005).

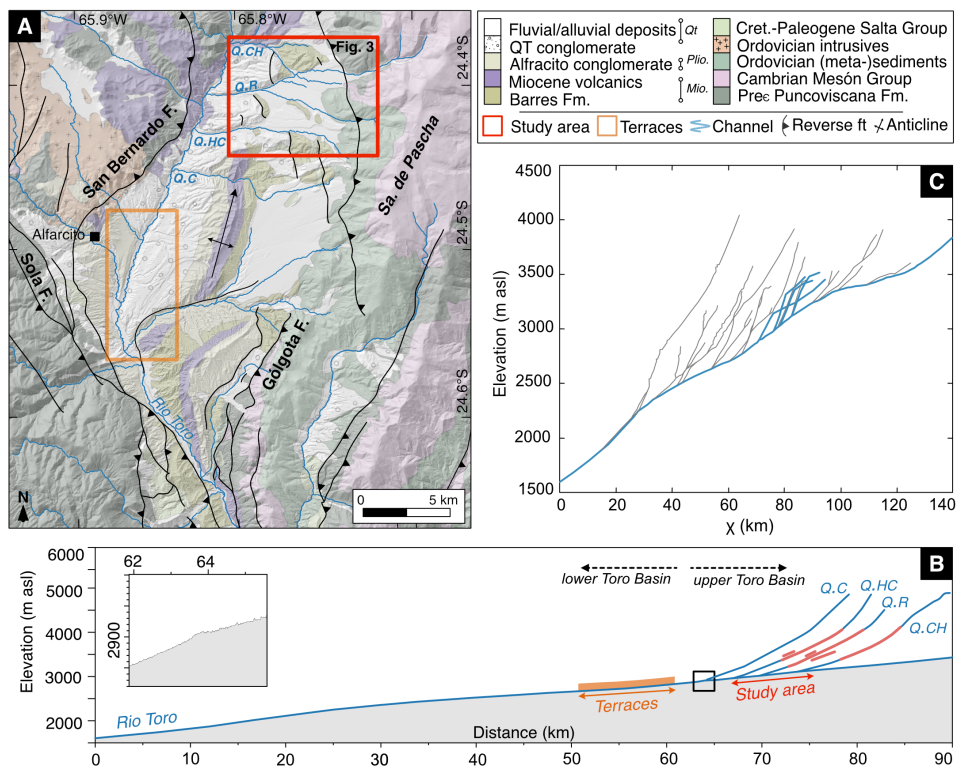
136

137 This study focuses on a suite of fans that emerge from the tributary catchments of the Sierra de Pascha  
138 and are located ~30 km upstream from the cut-and-fill terraces recording 100-kyr climate cyclicity  
139 described by Tofelde et al. (2017). The Pascha Ranges are characterised by meta-sediments of the Late  
140 Proterozoic-Cambrian Puncoviscana Formation and quartzites and shales of the Cambrian Mesón





141 Group (Schwab and Schafer 1976; García et al., 2013). Long term rock-uplift rates based on structural  
 142 reconstructions range between 0.4 and 0.6 mm/yr (Hilley and Strecker 2005).  
 143



144  
 145 **Figure 2.** Geology and topography of the upper Toro Basin. A) Geologic map with the alluvial fan sequence location (our  
 146 study area, Fig. 3) and cut-and-fill terraces described by Tofelde et al. (2017) outlined by red and orange rectangles  
 147 respectively. Other terraces extend discontinuously along the basin’s channel length but remain undated. Map adapted from  
 148 Segemar 250k geological maps and Pingel et al. (2020). Abbreviations: Sa. – Sierra, F – Fault, Q.CH – Quebrada (mountain  
 149 stream) Chacha Huaico, Q.R – Quebrada Rosal, Q. HC – Quebrada Huasa Ciénaga, Q.C – Quebrada del Chorro, Q.Ca –  
 150 Quebrada Carachi. B) Long profile of Toro Basin with tributary profiles of upper basin study area. Upper and lower basin  
 151 reaches are indicated by dashed arrows. Full basin profile extracted from fluvial network outlined in Fig. 1. Alluvial fan and  
 152 terrace surfaces are projected onto profiles. Inset: Higher resolution plot of proposed knickzone at confluence between the Río  
 153 Toro and Quebrada del Chorro (outlined in main plot by black box). C) Chi-plot of all channels with a minimum drainage area  
 154 of 1 km<sup>2</sup> within the Toro basin using a reference concavity index of 0.45. Bold lines highlight the main river channel and  
 155 tributary catchments within our study area.  
 156

157 The Middle Miocene Barres Sandstone, interbedded with lava flows, and the Pliocene-Pleistocene  
 158 Alfarcito Conglomerates are exposed along a north-trending anticline, which lies between the fan  
 159 deposits and the Río Toro (Fig. 2A; Mazzuoli et al., 2008; DeCelles et al., 2011; Robledo et al., 2020).  
 160 Resistant Barres and Alfarcito units characterise several erosional surfaces that stand ~700 m above the  
 161 modern river channel. Incision into these tectonically deformed units by tributaries draining the Sierra  
 162 de Pascha is thought to have occurred after 0.98 Ma (Hilley and Strecker, 2005), the age of an  
 163 intercalated ash unit dated from the uppermost layers of the Alfarcito Conglomerate (Marrett et al.,



164 1994). Undeformed Quaternary conglomerates (also called ‘Terrace Conglomerates’) and  
165 fluvial/alluvial deposits either mantle or infill this tectonically deformed and eroded palaeotopography  
166 (Fig. 2; Marrett and Strecker, 2000; Hilley and Strecker, 2005). The Río Toro sets the local base level  
167 for the Pascha tributaries today (Tofelde et al., 2017).

168

## 169 **2.2 Climatic setting**

170 Moisture mainly governed by the South American Summer Monsoon (SASM) system is directed by the  
171 South American low-level jet (SALLJ) from the Atlantic Ocean and Amazon Basin to the Central Andes  
172 (Vera et al., 2006; Alonso et al., 2006; Bookhagen and Strecker 2008; Castino et al., 2017). The semi-  
173 arid Toro Basin is located towards the southern limit of this moisture conveyor and receives rainfall that  
174 ranges from ~900 mm/yr at the outlet to < 200 mm/yr in the basin headwaters (Fig. 1; Bookhagen and  
175 Strecker 2008). The Sierra de Pascha acts as an orographic barrier, causing the eastern flanks of the  
176 range to be comparatively wetter than the basin interior. The intensity of the SASM and resultant  
177 moisture supply to the Central Andes has been variable over time (see Baker and Fritz, 2015 for detailed  
178 review). Paleoenvironmental records from Argentina, Chile and Bolivia show that SASM precipitation  
179 has varied with changes in insolation over 19 to 25-kyr (precession) (Godfrey et al., 2003, Fritz et al.,  
180 2004, 2010; Placzek et al., 2006; Bobst et al., 2001) and 100-kyr (eccentricity) (Fritz et al., 2007;  
181 Gosling et al., 2008) cycles. The Central Andes are also subject to increased rainfall during periods of  
182 northern hemispheric cooling, whereby the Atlantic part of the intertropical convergence zone (ITCZ)  
183 is forced southward, bringing moisture with it (Broccoli et al., 2006; Mosblech et al., 2012; Novello et  
184 al., 2017; Crivellari et al., 2018). These cold and wet conditions correlate with phases of glacial advance  
185 and rising lake levels (Haselton et al., 2002; Vizy and Cook, 2007; Martin et al., 2018; Mey et al., 2020).

186

187 Successions of glacial moraines are preserved within the Sierra de Pascha tributary catchments and are  
188 indicative of repeated late Quaternary glaciations (Tofelde et al., 2018). Glacial records proximal to the  
189 Toro Basin (24-27.2°S) underline the sensitivity of Andean glaciers to SASM precipitation intensity  
190 and temperature (Martini et al., 2017; Zech et al., 2017; Luna et al., 2018; D’Arcy et al., 2019a; Mey et  
191 al., 2020). The timing of regional glacial stages is invariably in phase with insolation cycles, periods of  
192 SASM strengthening and/or northern hemispheric events (e.g., Younger Dryas, Last Glacial Maximum)  
193 (D’Arcy et al., 2019a).

194

## 195 **2.3 Basin sediment infilling and incision**

196 Thick successions of sediment, together with subtle knickzones and hairpin turns in the Río Toro reflect  
197 a complex late Cenozoic history of basin filling and evacuation (Strecker et al., 2009; Hain et al., 2011;  
198 Vezzoli et al., 2012; Pingel et al., 2020), base level perturbations and tectonic deformation (Marrett and  
199 Strecker, 2000; Hilley and Strecker, 2005; Tofelde et al., 2017), and drainage reorganization (Seagren



200 and Schoenbohm, 2021; Seagren et al., 2022). Given our interest in the Quaternary deposits of the upper  
201 Toro Basin, we focus our attention on how the basin has evolved over the last one million years.

202

203 After deposition of the Alfarcito conglomerates concluded at ca. 0.98 Ma, the Toro Basin was evacuated  
204 to a base level lower than today (Hilley and Strecker, 2005). Renewed hydrological connectivity  
205 between the Toro Basin and the Lerma Valley likely caused widespread basin sediment evacuation and  
206 incision of the (paleo)topography. Uplift of the Sierra de Pascha Sur also recommenced sometime after  
207 ca. 0.98 Ma (Hilley and Strecker, 2005). The newly uplifted range impeded the delivery of precipitation  
208 to the basin interior, and by ca. 0.8 Ma, the semi-arid conditions of today were established (Kleinert and  
209 Strecker 2001; Strecker et al. 2007; Pingel et al., 2020). The mechanically strong basement rocks, and  
210 a potentially reduced sediment transport capacity, meant that incision was unable to keep pace with the  
211 renewed rock uplift. This forced widespread aggradation and a decrease in relief upstream of the  
212 Gólgota fault, and channel steepening within the bedrock gorge cutting through the Sierra de Pascha  
213 Sur (Fig. 2; Hilley and Strecker, 2005; Strecker et al., 2009; García et al., 2013). External drainage  
214 either became restricted or ceased at this time (Marrett et al. 1994; Hain et al., 2011; Pingel et al.,  
215 2019a). Evidence for a similar sequence of events is seen in the Humahuaca, Casa Grande and  
216 Calchaquí basins (23°S), where renewed range uplift reduced hydrological connectivity and caused  
217 sediment infilling (Robinson et al., 2005; Hain et al., 2011; García et al., 2013; Pingel et al., 2013, 2016,  
218 2019a; Streit et al., 2017; Seagren et al., 2022). Although there are some uncertainties about the exact  
219 timing, connectivity between the Toro Basin and the foreland is thought to have been re-established due  
220 to external base-level change (Seagren and Schoenbohm, 2021).

221

222 The Quaternary “Terrace Conglomerates” were deposited within the Toro Basin starting from ca. 0.94  
223 Ma and are considered part of this phase of uplift-induced basin infilling (Hilley and Strecker, 2005). A  
224 flight of six fluvial terrace levels in the lower basin are preserved between 20 and 200 m above the  
225 modern Río Toro (Fig. 2). Cosmogenic exposure-age dating of terraces, burial dating of the sediments,  
226 and zircon U-Pb ages of intercalated ashes from the terrace levels revealed multiple 100-kyr cut-and-  
227 fill sedimentary cycles starting from ca. 500 ka (Tofelde et al., 2017). The phases of incision correspond  
228 with cold, wet glacial periods, when sediment transport capacity apparently exceeded sediment flux,  
229 whereas aggradation occurred when sediment transport was considerably reduced (Tofelde et al., 2017).  
230 Moreover, the calculated net incision rate through the terrace sequence of 0.4 mm/yr from ca. 500 ka is  
231 consistent with long term rock-uplift rates of the Sierra de Pascha Sur at the basin outlet (Hilley and  
232 Strecker, 2005). Tofelde et al. (2017) thus concluded that while the renewed uplift of the Sierra de  
233 Pascha Sur helped initiate the deposition of the Terrace Conglomerates, the periodicity of the cut-and-  
234 fill cycles is best explained by orbitally driven climate forcing, with net incision likely associated with  
235 the channel response to ongoing rock-uplift. Today, catchment-averaged erosion rates for catchments  
236 draining the Sierra de Pascha range between <0.03 and 0.12 mm/yr (Tofelde et al., 2018).



237

### 238 **3. Methodology**

239

240 To evaluate past channel behaviour and landscape response to climate and/or tectonic forcing for the  
241 upper Toro Basin, we applied CRN exposure dating to the suite of fan surfaces along the western front  
242 of the Sierra de Pascha (Fig. 1, 2).

243

244 Alluvial fan CRN ages record the timing of active sediment deposition or surface stability between  
245 periods of channel avulsion and incision (Dühnforth et al., 2007; D’Arcy et al., 2019b), which lead to  
246 abandonment of the fan surface. This abandonment can occur due to changes in sediment supply  
247 (Brooke et al., 2018; Tofelde et al., 2019), tectonic deformation and base level change (Ganev et al.,  
248 2010; Mouslopoulou et al., 2017), climate-induced changes in water discharge (Steffen et al., 2010;  
249 Savi et al., 2016) or drainage reorganization (Bufe et al., 2017). Because fan surfaces can remain active  
250 for  $10^{2-5}$  years before being incised (Cesta and Ward, 2016; Dühnforth et al., 2017; Ratnayaka et al.,  
251 2019; Peri et al., 2022), the age distribution or minimum exposure age of boulders on an alluvial fan  
252 surface will not necessarily tightly constrain the timing of abandonment. Instead, the distribution of  
253 CRN ages, after excluding clear outliers, more likely reflects phases of fan activity, and at best, provide  
254 a minimum age limit for the onset of incision leading to eventual surface abandonment (D’Arcy et al.,  
255 2019b).

256

257 We mapped the upper Toro Basin fans using TanDEM-X (12 m-resolution) data and Google Earth  
258 imagery. The stratigraphic relationships among the different fan surfaces were used to inform the  
259 cosmogenic radionuclide (CRN) sampling strategy (e.g., McFadden et al., 1989; Hughes et al., 2010;  
260 Hedrick et al., 2013).

261

262 Supporting topographic, fan and channel data were extracted from the DEM using TopoToolbox  
263 functions in MATLAB (Schwanghart and Scherler, 2014) and geospatial toolboxes (GRASS, GDAL)  
264 in QGIS. We also compiled a set of climate (Berger and Loutre, 1991; Baker et al., 2001; Imbrie et al.,  
265 2006; Fritz et al., 2007; Wang et al., 2007; Lisiecki and Raymo, 2009), paleoenvironmental (Hilley and  
266 Strecker, 2005; Tofelde et al., 2017; Pingel et al., 2020), glacial (Martini et al., 2017; Zech et al., 2017;  
267 Luna et al., 2018; D’Arcy et al., 2019a; Mey et al., 2020) and geomorphic (Terrizzano et al., 2017;  
268 Tofelde et al., 2017; Pingel et al., 2019b; Tobal et al., 2021; Peri et al., 2022; Milanez Fernandes, 2023)  
269 records for the Andes to help contextualise our results.

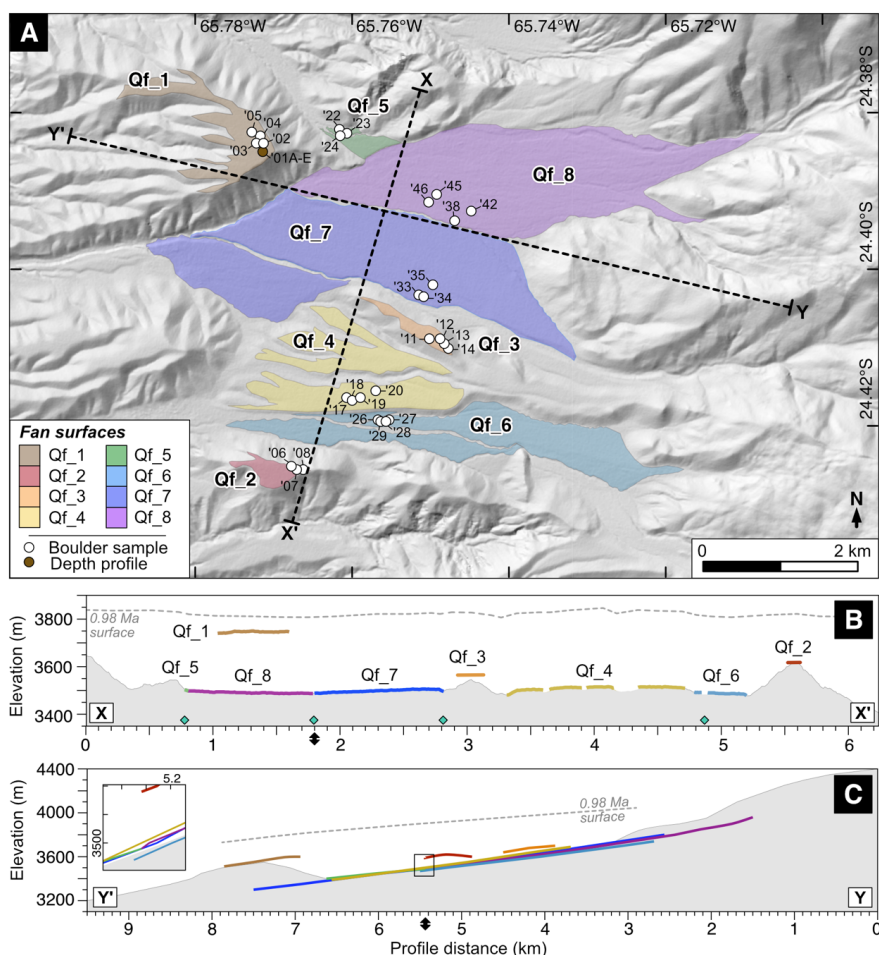
270

#### 271 **3.1 CRN dating**

272 We collected a total of 30 quartzite boulder surface samples from eight fan surfaces (Fig. 3). Between  
273 three and four boulders were sampled per surface. Each surface was named ‘Qf’ for ‘Quaternary fan’,



274 followed by a number which referred to its stratigraphic position. For example, Qf\_1 sits ~200 m above  
 275 the modern river channel, and as the highest elevation surface of the study area, it was anticipated to be  
 276 the oldest fan.  
 277



278  
 279 **Figure 3.** Alluvial fan surfaces of the upper basin. A) Hillshade map of the dated fan surfaces with boulder and depth profile  
 280 sampling locations shown. Sample names have been abbreviated (e.g.: TB19\_05: '05). X-X' and Y-Y' projection lines of Fig.  
 281 3B and 3C are represented by dashed black lines. B) Fan sequence stratigraphy shown by fan surfaces projected onto X-X'.  
 282 Qf\_2 and Qf\_3 surface widths are slightly exaggerated to improve visibility. Modern topography shaded in grey. The 0.98Ma  
 283 surface (grey dashed line) is modelled from sediment evacuation estimates of Hilley and Strecker (2005). Location of active  
 284 fluvial channels indicated by green diamond symbol. C) Fan surfaces projected onto Y-Y'. Inset plot provides higher resolution  
 285 view of projections (outlined by black rectangle). Projection line intersection is indicated by black double arrow.  
 286

287 Each sampled boulder was embedded within the fan surface, located away from channels, and within  
 288 the distal zone of the landform. This sampling strategy reduced the likelihood that the boulders were  
 289 sourced from adjacent hillslopes or were part of a depositional event following landform abandonment  
 290 (D'Arcy et al., 2019b; Orr et al., 2021). The sampled boulders were the largest, freshest boulders that





291 we were able to identify within the distal zone. However, we cannot definitively discount the possibility  
292 that the boulders experienced some weathering, surface spallation or fracturing in the past.

293

294 We removed between 400 and 1000 g of sample from the upper three centimetres of each boulder  
295 surface. The samples were crushed and then sieved to isolate the 250–500  $\mu\text{m}$  grainsize fraction needed  
296 for CRN dating. Sample cleaning, purification, extraction and oxidation of  $^{10}\text{Be}$ , and target preparation  
297 for AMS measurement was conducted in the Helmholtz Laboratory for the Geochemistry of the Earth  
298 Surface (HELGES) at the German Research Centre for Geosciences (GFZ-Potsdam) using the  
299 procedures outlined by von Blanckenburg, (2004) and Wittmann et al. (2016). AMS measurements were  
300 completed at the Cologne AMS facility at the University of Cologne, Germany.

301

302 Exposure ages derived from *in situ* produced  $^{10}\text{Be}$  concentrations were calculated using the CREP online  
303 calculator (Martin et al., 2017) with the regional reference (SLHL) production rate of  $3.74 (\pm 0.09)$  at/  
304  $\text{g yr}$  for the high-elevation ( $> 3400$  m asl) Central Andes (Blard et al., 2013; Kelly et al., 2015; Martin  
305 et al., 2015), and the LSD scaling scheme (Lifton et al., 2014). Further information about the boulder  
306 samples, the CRN laboratory procedure, blank ratios, and age calculation is provided in Supplement 1  
307 and 2.

308

309 The probabilistic model for inferring the timing of fan surface abandonment from D'Arcy et al. (2019  
310 b) was applied to fans with exposure ages of less than ca. 300 ka. The model uses the exposure ages of  
311 boulders on the fan surface to generate a probability distribution of abandonment ages and a most  
312 probable abandonment age. The model was not applied to older fan surfaces, which have large age  
313 distributions ( $>100$  kyr range) and likely have some inheritance and/or surface erosion (Phillips et al.,  
314 1990; Tobal et al., 2021). Working with chronological data at this coarse resolution over  $10^{5-6}$ -year  
315 timescales means that even the most sophisticated inheritance/erosion models are limited in their ability  
316 to estimate the timing of landform abandonment (e.g., Prush and Oskin, 2020; Dortch et al., 2022). For  
317 the Toro fans where this applies, we use the age distribution, stratigraphic order of the fans, and youngest  
318 exposure age as a guide for the timing of abandonment.

319

### 320 3.2 $^{10}\text{Be}$ depth profile

321 To help substantiate our new  $^{10}\text{Be}$  boulder dataset we also resampled the Qf\_1  $^{10}\text{Be}$  depth profile,  
322 referred to as P6b by Tofelde et al. (2017), and corresponding to their terrace level T6. The original  
323 profile was limited to five samples, which were sampled over relatively broad depth intervals (0–10cm,  
324 18–28 cm, 25–81 cm, 82–164 cm, 164–210 cm). To obtain more highly resolved  $^{10}\text{Be}$  data for this  
325 surface, particularly in the upper 100 cm, five samples of  $> 65$  pebbles each were extracted from the  
326 following depth intervals (cm): 0–10, 20–30, 40–50, 60–70 and 115–125. The pebble samples were



327 crushed and sieved, and the 500–1000  $\mu\text{m}$  fraction was reserved for CRN dating. Subsequent laboratory  
328 procedures followed that of the boulder samples.

329

330 The Qf\_1  $^{10}\text{Be}$  depth profile, using combined  $^{10}\text{Be}$  data from this study and from Tofelde et al., (2017),  
331 was used to determine an exposure age using the Hidy et al. (2010) Monte Carlo simulator. Further  
332 details are provided in Supplement 1 and 2.

333

#### 334 4. Results

335

336 We use the upper Toro Basin alluvial fan elevations, surface characteristics, and CRN ages to identify  
337 two generations of fan surfaces. The studied fans are predominantly matrix-supported conglomerates  
338 with sub-angular to rounded pebble and cobble clasts. Weathered desert pavements cap many of the fan  
339 surfaces; a layer of finer sands and gravels are overlain by pebbles, cobbles, and boulders (e.g.,  
340 McFadden et al., 1989; Tofelde et al., 2017).

341

342 The Generation 1 (G1) fan surfaces, comprising Qf\_1 through 4, are stratigraphically the highest in the  
343 record and are positioned ~200 to 50 m above the modern river channel(s) (Fig. 3). The fan surfaces are  
344 moderately to highly weathered, with some evidence of surface boulder spallation (Fig. 4). With a few  
345 rare exceptions, the G1 sampled boulders are smaller than those sampled from the lower Generation 2  
346 (G2) surfaces. The G1 and G2 boulders have b-axis lengths which range from 30 to 80 cm and 30 to  
347 140 cm, respectively (Supplement 2). The CRN exposure ages from the G1 surfaces range between ca.  
348 970 and 340 ka (Table 1; Fig. 5, 6).

349

350 G2 is comprised of fans Qf\_5 through 8, which have surfaces within 10 m elevation of the modern  
351 channel(s) (Fig. 3). These moderately weathered surfaces retain debris flow deposits, evidence of past  
352 channel avulsion and sparse human infrastructure (e.g., stone walls). The CRN exposure ages of this  
353 younger fan generation range between ca. 100 and 20 ka, with estimated surface abandonment ages  
354 after ca. 70 ka (Table 1; Fig. 7).

355

356

357

358

359

360

361

362



**Table 1.** Sample properties, measured <sup>10</sup>Be concentrations and calculated exposure ages of each sampled boulder from the Toro fans. Further sample and age calculation details are provided in the Supplement 2 and 3.

Sample	Location		Elevation (m asl)	Sample thickness (cm)	Shielding correction	Be-10 concentration		Be-10 exposure ages	
	Latitude (°S)	Longitude (°W)				Concentration (10 <sup>6</sup> at/g SiO <sub>2</sub> )	Uncertainty (10 <sup>6</sup> at/g SiO <sub>2</sub> )	Age (ka)	Uncertainty (ka)
<b>Qf_1</b>									
TB19_02	-24.38492	-65.76890	3556	1	0.990	24.20	0.78	966.63	109.78
TB19_03	-24.38492	-65.76890	3556	1	0.990	16.02	0.52	593.11	59.10
TB19_04	-24.38492	-65.76890	3556	1	0.990	22.33	0.72	884.41	95.34
TB19_05	-24.38492	-65.76890	3556	1	0.990	16.97	0.55	639.17	63.94
<b>Qf_2</b>									
TB19_06	-24.42522	-65.76775	3560	1	0.999	11.36	0.37	391.94	37.91
TB19_07	-24.42566	-65.76682	3570	2	0.999	17.00	0.55	631.77	64.10
TB19_08	-24.42568	-65.76607	3581	2	0.999	10.18	0.33	336.94	33.17
<b>Qf_3</b>									
TB19_11	-24.40882	-65.75023	3644	1	0.998	15.45	0.50	533.56	52.88
TB19_12	-24.40918	-65.74864	3658	3	0.998	18.06	0.59	651.82	66.21
TB19_13	-24.40976	-65.74810	3660	3	0.998	17.77	0.58	634.67	64.63
TB19_14	-24.41011	-65.74773	3673	3	0.998	11.18	0.37	361.38	35.49
<b>Qf_4</b>									
TB19_17	-24.41665	-65.76059	3509	1	0.999	14.73	0.48	548.44	54.60
TB19_18	-24.41675	-65.76000	3512	2	0.999	17.26	0.56	679.67	68.23
TB19_19	-24.41654	-65.75923	3519	3	0.999	19.06	0.61	778.81	79.15
TB19_20	-24.41533	-65.75681	3541	1	0.999	21.41	0.69	847.34	90.30
<b>Qf_5</b>									
TB19_22	-24.38245	-65.76145	3404	2	0.990	2.02	0.07	70.63	6.28
TB19_23	-24.38263	-65.76109	3407	2	0.995	2.34	0.08	82.69	7.35

363  
364  
365



TB19_24	-24.38275	-65.76144	3405	3	0.995	2.77	0.09	98.81	8.82
<b>Qf_6</b>									
TB19_26	-24.41923	-65.75623	3531	2	0.998	2.16	0.07	69.97	6.27
TB19_27	-24.41921	-65.75578	3532	1	0.998	2.52	0.08	81.85	7.31
TB19_28	-24.41924	-65.75569	3541	2	0.998	2.22	0.08	71.11	6.46
TB19_29	-24.41941	-65.75652	3525	3	0.998	2.47	0.08	82.00	7.33
<b>Qf_7</b>									
TB19_33	-24.40346	-65.75108	3557	1	0.998	1.22	0.04	38.78	3.46
TB19_34	-24.40371	-65.75107	3555	2	0.998	1.87	0.06	59.28	5.36
TB19_35	-24.40203	-65.74977	3563	3	0.998	2.11	0.07	66.94	6.13
<b>Qf_8</b>									
TB19_38	-24.39402	-65.74711	3533	1	0.997	1.43	0.05	44.34	4.08
TB19_42	-24.39275	-65.74500	3553	1	0.997	1.43	0.05	43.65	4.04
TB19_45	-24.39043	-65.74940	3510	1	0.997	0.63	0.02	22.37	1.85
TB19_46	-24.39140	-65.75027	3502	1	0.997	1.44	0.05	45.32	4.212

366 I: LSD scaling scheme (Lifton et al., 2014), ERA40 Atmosphere Model (Uppala et al., 2005), LSD framework for geomagnetic correction (Lifton et al., 2014), Reference (SLHL) production  
 367 rate: 3.74+0.09 at/g/yr. Sample density: 2.75 g cm<sup>-3</sup>. Erosion: 0 mm yr<sup>-1</sup>  
 368

369

370

371

372

373

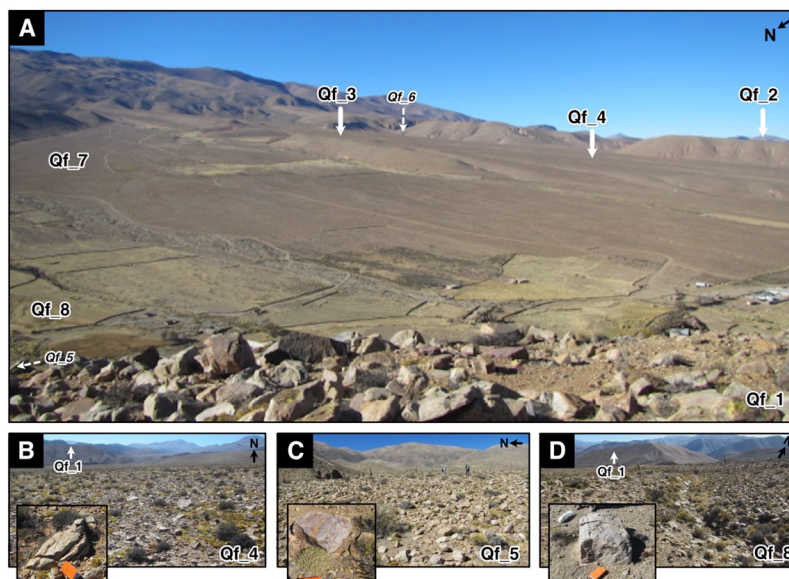
374

375

376



377



378

379 **Figure 4.** Images of the alluvial fan sequence of the upper Toro Basin. A) Image taken from Qf\_1 surface (facing SE) with  
 380 fan surfaces labelled. Italicized text with arrows indicates location of surfaces that are not clearly in shot. B) Qf\_4 surface.  
 381 Inset image of sampled boulder TB19\_19. C) Qf\_5 surface. Inset image of sampled boulder TB19\_22. D) Qf\_8 surface. Inset  
 382 image of sampled boulder TB19\_44. Images B–D encompass full age range of sampled surfaces. Further images of the fan  
 383 surfaces and  $^{10}\text{Be}$  samples are provided in Supplement 3.

384

#### 385 4.1 Generation 1

386 Qf\_1 is the highest fan surface of the record (~200 m above the modern channel), which extends from  
 387 the Quebrada Rosal tributary catchment. The fan comprises part of the Quaternary conglomerates,  
 388 which overlie the Barres Sandstone Formation (Fig. 2, 3). The depth profile is composed of four  
 389 sedimentary units that coarsen with depth: silts and fine sands (0–20 cm), fine-coarse sand (20–60 cm),  
 390 coarse sand and gravel (60–180 cm) and gravels (>180 cm). Consistent with the original profile, the  
 391 new  $^{10}\text{Be}$  sample concentrations decrease exponentially with depth (Fig. 5; Table 2). Qf\_1 has a  
 392 Bayesian most-probable exposure age of  $715.8^{+35}_{-217}$  ka ( $2\sigma$  upper age: 750.8 ka,  $2\sigma$  lower age: 498.8  
 393 ka) and  $0.26 \pm 0.42 \times 10^6$  atoms/g of inheritance. Within the simulator, we constrained fan surface erosion  
 394 and inflation by setting the erosion rate to range between -0.02 and 0.2 cm/ka and using maximum and  
 395 minimum erosion thresholds of -10 and 50 cm, respectively. While this modelled exposure age is  
 396 consistent with the age estimated earlier by Tofelde et al. (2017) of  $732^{+53}_{-56}$  ka assuming a stable  
 397 surface, or  $644^{+43}_{-49}$  ka accounting for surface inflation, Tofelde et al. (2017) preferred the exposure  
 398 age they derived from surface pebbles of  $453 \pm 33$  ka.

399

400 The exposure ages of boulder samples TB19\_03 and TB19\_05 are in agreement with the depth profile  
 401 results, yielding exposure ages of  $639.17 \pm 63.94$  and  $593.11 \pm 59.10$  ka ( $2\sigma$  uncertainty). The two





402 remaining boulders (TB19\_02, TB19\_04) yielded older exposure ages of  $966.63 \pm 109.78$  and  $884.41$   
 403  $\pm 95.34$  ka.

404

405 **Table 2.** Sample depths and measured  $^{10}\text{Be}$  concentrations of Qf\_1 depth profile. Fan age calculated with the Hidy  
 406 et al. (2010) Monte Carlo depth profile simulator was  $715.8^{+35/-217}$  ka. Inheritance measured:  $0.26 \pm 0.42 \times 10^6$  at/g.  
 407

Sample <sup>1</sup>	Sample depth		Be-10 concentration	
	Depth (cm)	Uncertainty (cm)	Concentration ( $10^6$ at/g $\text{SiO}_2$ )	Uncertainty ( $10^6$ at/g $\text{SiO}_2$ )
BBC-0	5	5	14.70	0.18
TB19_01A	5	5	14.97	0.48
BBC-1	23	5	11.80	0.11
TB19_01B	25	5	12.14	0.39
TB19_01C	45	5	10.88	0.35
BBC-2	53	28	7.76	0.07
TB19_01D	65	5	8.76	0.28
TB19_01E	120	5	4.94	0.16
BBC-3	123	41	5.21	0.06
BBC-4	187	23	2.30	0.03

408 <sup>1</sup>: TB19\_01A-E from this study. 'BBC-1-4' from Tofelde et al. (2017).  
 409

410 Surface Qf\_2, the second highest surface (ca. 130 m above the closest modern channel), also overlies  
 411 the Barres Sandstone and likely extends from the Quebrada Huasa Ciénaga and Quebrada del Chorro  
 412 catchments. CRN exposure ages from three boulders range from  $631.88 \pm 64.10$  to  $336.94 \pm 33.17$  ka.

413

414 The Qf\_3 surface is positioned ca. 60 m above the closest modern channel and extends from the  
 415 Quebrada Rosal tributary catchment. The surface yields three CRN boulder exposure ages that cluster  
 416 between  $651.82 \pm 66.21$  and  $533.56 \pm 52.88$  ka, and one younger age of  $361.38 \pm 35.49$  ka.

417

418 Qf\_4 has a highly dissected fan surface which is the lowest stratigraphically of the G1 fans; the fan is  
 419 positioned ca. 40 m below the Qf\_3 surface and ca. 30 m elevation above the modern channel. Four  
 420 boulder exposure ages range from  $911.61 \pm 100.27$  to  $548.44 \pm 54.60$  ka.

421

## 422 4.2 Generation 2

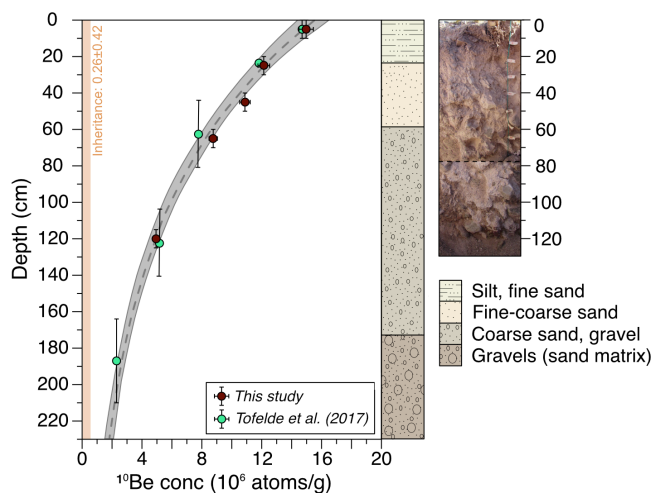
423 Qf\_5 is a small G2 surface that sits ca. 10 m above the neighboring Qf\_8 fan. Qf\_5 has three exposure  
 424 ages that range from  $98.81 \pm 8.82$  to  $70.63 \pm 6.28$ ka, with a most probable abandonment age of  $61.8$   
 425  $^{+13.5}_{-33.6}$  ka (no ages excluded as outliers).

426

427 Qf\_6's surface is characterized by moderately weathered debris flow deposits with clusters and  
 428 elongated ridges of boulders. Exposure ages range between  $82.00 \pm 7.33$  and  $69.97 \pm 6.27$  ka from the



429 four boulders, with an estimated surface abandonment age of  $66.2^{+11.0}_{-17.5}$  ka (no ages excluded as  
 430 outliers).



431

432 **Figure 5.**  $^{10}\text{Be}$  concentration with depth for Qf\_1 profile alongside sedimentary log and stitched field image of the profile pit.  
 433 Each sample was collected over a depth range represented by a vertical error bar. Horizontal error bar represents the  $1\sigma$   
 434 analytical uncertainty for the nuclide concentration. The Hidy et al. (2010) Monte Carlo simulator fit 100,000 curves (grey  
 435 shading) to profile and generated most probable fit (grey dashed line). Modelled inheritance is shown by orange line. \*Profile  
 436 6b data, rather than 6a, from the supplementary materials is used in simulation, due to the mislabelling of the profile in Fig. 4  
 437 of Tofelde et al. (2017).  
 438

439 Despite Qf\_7 being located within 5 m elevation of the youngest G2 fan Qf\_8, this large fan appears  
 440 more weathered than Qf\_8. Qf\_7 has CRN exposure ages of  $66.94 \pm 6.13$ ,  $59.28 \pm 5.35$  and  $38.78 \pm$   
 441  $3.47$  ka. The surface abandonment ages including and excluding the youngest age are  $33.9^{+7.4}_{-25.1}$  and  
 442  $52.9^{+11.0}_{-16.3}$  ka, respectively.

443

444 Surface Qf\_8 yielded a cluster of older ages that range between  $45.32 \pm 4.2$  and  $43.65 \pm 4.04$  ka and a  
 445 single younger age of  $22.37 \pm 1.83$  ka. Abandonment ages including and excluding the youngest age  
 446 are  $19.4^{+4.1}_{-19.4}$  and  $42.4^{+6.5}_{-7.5}$  ka, respectively. The surface is covered with relatively unweathered  
 447 debris flow deposits and large varnish-free boulders.

448

## 449 5. Discussion

450

451 While there are some nuances to the Toro Basin fan record, our new CRN dataset enables us to identify  
 452 significant phases of net incision since ca. 0.98 Ma, capture the channel response to external forcing  
 453 over a range of timescales and cyclicities, and gain further insight into the late Quaternary evolution of  
 454 the Toro Basin.

455



456 **5.1 Timing of alluvial fan development and abandonment**

457 CRN age uncertainties on the order of  $10^{+5}$  years and a wide range of fan exposure age distributions on  
458 individual surfaces present some challenges when interpreting the Toro fan chronostratigraphy, which  
459 is crucial for comparison with potential external forcing conditions. Constraining the geological  
460 uncertainties of the CRN ages, particularly for old fan surfaces, is often challenging (Owen et al., 2014).  
461 For this reason, we use geological, topographic and paleoenvironmental data alongside the  $^{10}\text{Be}$  data to  
462 interpret the alluvial fan record. The coarse resolution of the G1  $^{10}\text{Be}$  record means that while we can  
463 reflect upon long term shifts in channel behaviour for the upper Toro Basin, we must exercise caution  
464 when linking this record to specific forcing or events (Gray et al., 2014; Dühnforth et al., 2017; Orr et  
465 al., 2021). Pairing the  $^{10}\text{Be}$  record with cosmogenic  $^{21}\text{Ne}$  in the future may help to decipher some of the  
466 complexities in the exposure histories of the boulders;  $^{21}\text{Ne}$  is well suited for quantifying long term  
467 landscape change in arid, low erosion environments (Dunai et al., 2005; Ma and Stuart, 2018).

468

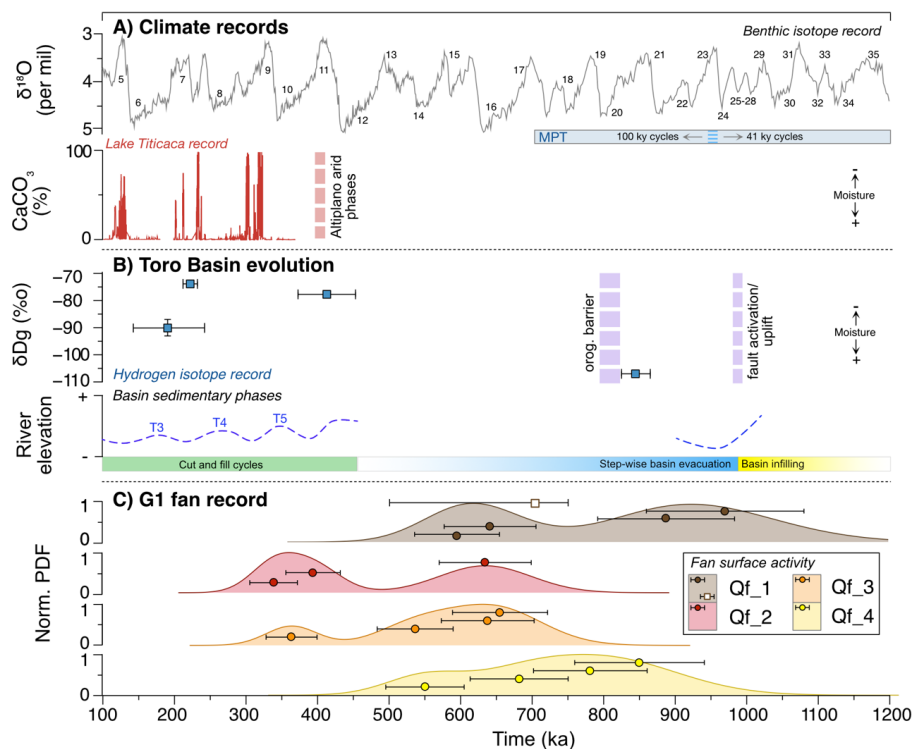
469 *5.1.1 Fan Generation 1*

470 The ~200-m elevation difference between the highest and lowest fan surface among Generation 1 means  
471 that the G1 surfaces could not have been active simultaneously (Fig. 6). Substantial inheritance and/or  
472 erosion has therefore likely affected individual boulders from these surfaces and offers one explanation  
473 for the broad spread in ages (>400 kyr) for each.

474

475 Pairing the Qf\_1  $^{10}\text{Be}$  depth profile with the surface boulder exposure ages means that we can more  
476 robustly constrain the oldest phase of fan development within the study area and use it as a benchmark  
477 when evaluating the remainder of the G1 fan record. The most recent phase of Qf\_1 surface activity  
478 and/or stability is constrained by the depth profile data and two boulders to between ca. 750 and 600  
479 ka. In this case, we believe that CRN inheritance may explain why the remaining two boulders  
480 (TB19\_02, TB19\_04) from this surface yield exposure ages that exceed ca. 800 ka. Considering the  
481 whole suite of boulder ages for the G1 fans, which mostly exceed 500 ka, we find it unlikely that the  
482 age of  $453 \pm 33$  ka (based on surface pebbles) originally reported by Tofelde et al. (2017) for Qf\_1 is  
483 correct.

484

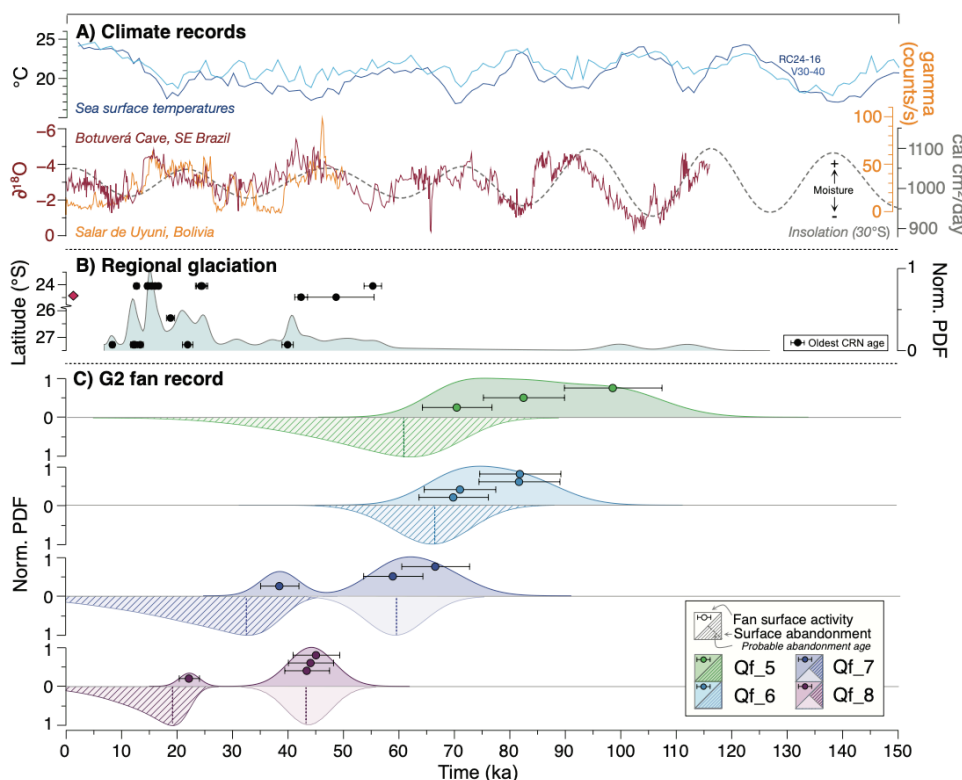


485 **Figure 6.** Comparison between the G1 fan  $^{10}\text{Be}$  dataset and records of Toro Basin evolution and climate. A) Benthic isotope  
 486 record (Lisiecki and Raymo 2009) displayed alongside Marine Isotope Stages (MIS) and Mid-Pleistocene Transition labelling  
 487 and the Lake Titicaca sediment core record ( $\text{CaCO}_3$  concentration) from Fritz et al. (2007). B) Toro basin evolution. Climatic  
 488 variability represented by hydrogen isotope record of Pingel et al. (2020). Basin sedimentary and tectonic phases plotted with  
 489 respect to inferred river elevation over time, as observed by this study and described by Hilley and Strecker (2005), Tofelde et  
 490 al. (2017) and Pingel et al. (2020). Fluvial terrace record (T3-6) from Tofelde et al. (2017). C)  $^{10}\text{Be}$  surface boulder ages and  
 491 normalised probability density functions of the G1 surfaces. Horizontal error bars represent the  $1\sigma$  uncertainty for the exposure  
 492 ages. Bayesian modelled surface age of Qf\_1 ( $715.8^{+35}_{-217}$  ka) derived from depth profile (Fig. 5) is denoted by square point.  
 493

494 Given the stratigraphic positions of Qf\_2 and Qf\_3, we think that it is unlikely that active streams were  
 495 present on these surfaces after ca. 400 ka. For this reason, we suggest that the younger ages for these  
 496 surfaces are the result of erosion. These surfaces also must be older than surface Qf\_4, which yielded a  
 497 youngest age of ca. 550 ka.

498

499 Inheritance also likely explains the old ( $>750$  ka) boulders on Qf\_4, which is stratigraphically younger  
 500 than Qf\_1 and cannot have been active at the same time.



501

502 **Figure 7.** Comparison between the G2 fan  $^{10}\text{Be}$  dataset and regional climate and glacial records. A) Climate records. Sea  
 503 surface temperatures from Imbrie et al. (2006), insolation from Berger and Loutre (1991), Botuverá Cave, SE Brazil  
 504 speleothem record from Wang et al. (2007) and Salar de Uyuni, Bolivia lake record from Baker et al. (2001). B) CRN glacial  
 505 chronologies from the Central Andes : Nevado de Chañi (24°S, 65.7°W, Martini et al., 2017, Mey et al., 2020), Quevar Volcano  
 506 (24.4°S, 66.8°W, Luna et al., 2018), Sierra de Quilmes (26.2°S, 66.2°W, Zech et al., 2017) and the Sierra Aconquija (27.2°S,  
 507 66.1°W, D’Arcy et al., 2019a). Location of Toro Basin (24.4°S, 66.7°W) is indicated by red diamond symbol. C)  $^{10}\text{Be}$  surface  
 508 boulder ages and normalised probability density functions of the G2 surfaces. Horizontal error bars represent the  $1\sigma$  uncertainty  
 509 for the exposure ages. Normalised PDF of fan surface abandonment (hashed shading) calculated using the D’Arcy et al.  
 510 (2019b) probabilistic model for fan surface abandonment. Surface abandonment for Qf\_7 and Qf\_8 without youngest boulder  
 511 ages (TB19\_33 and TB19\_45, respectively) shown by PDFs with opaque solid shading. Most probable abandonment ages  
 512 denoted with dashed vertical lines- Qf\_5: 61.8  $^{+13.5}_{-33.6}$  ka, Qf\_6: 66.2  $^{+11.0}_{-17.5}$  ka, Qf\_7: ca. 33.9  $^{+7.4}_{-25.1}$  ka (52.9  $^{+11.0}_{-16.3}$   
 513 ka), Qf\_8: 19.4  $^{+4.1}_{-19.4}$  ka (42.4  $^{+6.5}_{-7.5}$  ka).  
 514

515 Given these complexities in the fan chronostratigraphy, rather than identifying discrete phases of  
 516 aggradation and incision for each fan surface, we suggest that the G1 fan record can instead be used to  
 517 capture an extended phase of net incision within the Sierra de Pascha tributaries. By comparing the G1  
 518 fan record with the modelled palaeotopography of Hilley and Strecker (2005), we estimate that ~100 m  
 519 of net incision (~0.01 mm/yr) occurred within the upper basin between ca. 0.98 Ma and 800 ka, at which  
 520 point the Qf\_1 surface became active (Fig. 3B, C, Fig. 8). Approximately 200 m of net incision (~0.07  
 521 mm/yr) then followed between ca. 800 ka and the complete abandonment of the G1 fans by ca. 500 ka  
 522 (when adjusting for age outliers) (Fig. 6), which signals the significant stepwise evacuation of sediment  
 523 from the upper Toro Basin at this time.

524





525 *5.1.2 Fan Generation 2*

526 The G2 record reveals that after a hiatus in the geomorphic record ca. 500 and 100 ka, fan aggradation  
527 and incision is recorded throughout several of the Sierra de Pascha tributaries (Fig. 8). Rather than  
528 recording continuous fan activity since ca. 110ka, the distribution of ages for G2 instead likely captures  
529 multiple distinct phases of deposition. The G2 fan surfaces have much tighter constrained age  
530 distributions (ca. 21 to 40 kyr) compared to the G1 fans, with two G2 fans showing what may be young  
531 outliers; the boulders are therefore less likely to be affected by inheritance, but the young outliers may  
532 be affected by erosion or tilting by human or animal activity.

533

534 **5.2 Drivers of alluvial channel system change and fan/terrace formation**

535 Before we can explore some of the possible explanations for the alluvial system change recorded in the  
536 Toro Basin, we must first consider the specific local conditions needed to help explain the G1 (ca. 800  
537 to 500 ka) and G2 (ca. 100 to 20 ka) fan generations in the upper basin, as well as the fluvial terrace  
538 sequence (ca. 370 ka to <75 ka) in the lower basin. Changes in water or sediment discharge, governed  
539 by climate, can affect channel slopes and prompt adjustments to the channel bed elevations through  
540 incision or aggradation (Howard, 1982; Wickert and Schildgen, 2019; Tofelde et al., 2019).  
541 Nevertheless, net incision is essential to preserving the geomorphic record of aggradation-incision  
542 cycles. Otherwise, subsequent aggradational phases are likely to bury earlier landforms. Net incision  
543 can occur through the channel response to ongoing rock uplift or base level fall (Simpson and  
544 Castelltort, 2012), the latter of which may include renewed incision through an aggraded sequence of  
545 sediment downstream. While autogenic processes, such as channel avulsion and meander cut-offs may  
546 also play a role in channel incision and the formation of discrete fan lobes or terraces (Nicholas and  
547 Quine, 2007; Ventra and Nichols, 2014), we consider the scale of channel incision associated with the  
548 features of interest (ranging from ca. 10 to hundreds of meters) is beyond the scope of purely autogenic  
549 behavior. Below, we consider how climate-modulated changes to water and sediment discharge,  
550 together with events that can drive net incision, may have helped to generate, and preserve multiple  
551 generations of fans and terraces within the Toro Basin.

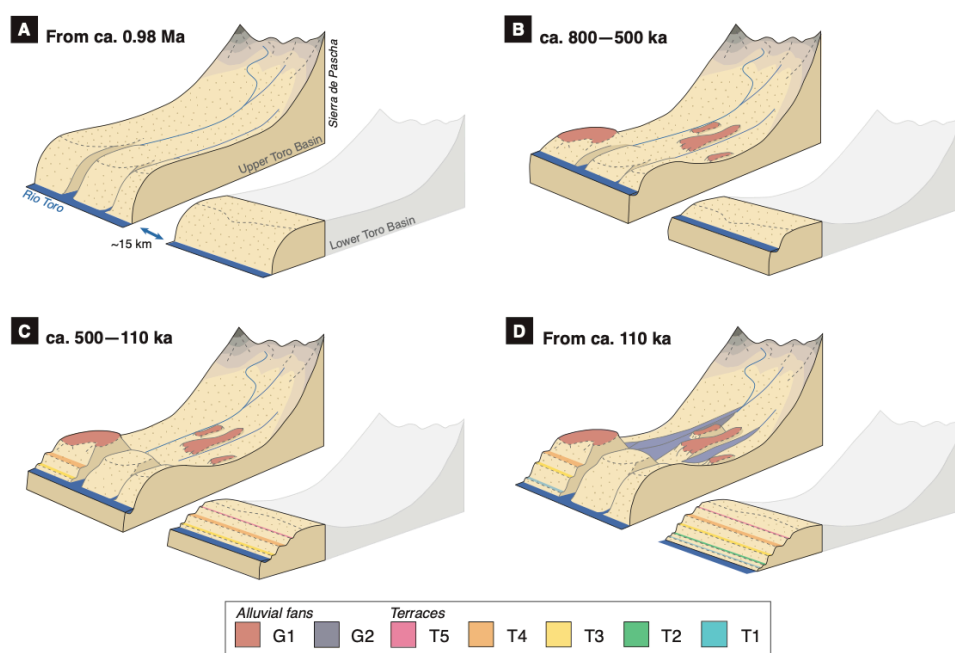
552

553 *5.2.1 Fan formation from ca. 800 to 500 ka*

554 The development, entrenchment, and eventual abandonment of the G1 fans could be part of the  
555 landscape response to enhanced rock-uplift of the Sierra de Pascha Sur, starting no later than ca. 800 ka  
556 (Fig. 8) (Clarke et al., 2010; Mather et al., 2017; Mouchené et al., 2017). However, another mechanism  
557 is likely at play because the averages rates of incision between ca. 800 and 500 ka (0.8 mm/yr) as  
558 recorded by the G1 fans, exceed the estimated rock uplift rates of 0.4 – 0.6 mm/yr (Hilley and Strecker,  
559 2005), and tectonic uplift alone is unlikely to be pulsed in a manner that would generate multiple fans.  
560 More likely, both climate forcing and tectonic forcing combine to produce and preserve the G1 fan  
561 sequence. Over the same period, curiously, no terraces are detected in the lower Toro Basin. Three



562 possible explanations for this absence (which are not mutually exclusive) include: (1) due to their more  
 563 central position within the basin, the lower reaches of the Río Toro were not strongly affected by rock  
 564 uplift, meaning that any changes in river-channel elevation are not persevered in the geomorphic record  
 565 due to low or a lack of net incision; (2) channels in the lower Toro Basin continued to experience  
 566 aggradation or remained stable at this time, due to feedbacks in the system whereby incision upstream  
 567 caused a pulse of sediment for downstream reaches; or (3) the response time of the Río Toro within the  
 568 lower basin was substantially longer than the forcing period of the aggradation-incision cycles, meaning  
 569 perturbations to the channel-bed elevation due to climate forcing would not have reached so far  
 570 downstream.  
 571



572  
 573 **Fig. 8.** Cartoon illustrating periods of aggradation and incision in the upper and lower Toro Basin from ca. 0.98 Ma. Area of  
 574 Lower Toro Basin block shaded in grey was not part of this study. A) From 0.98Ma: Base level lowered to present day levels,  
 575 following the deposition of Alfarcito Conglomerates. Renewed hydrological connectivity likely led to extensive sediment  
 576 evacuation and incision of (paleo)topography. Deposition of Quaternary Terrace Conglomerates started from 0.94 Ma (Hilley  
 577 and Strecker, 2005). B) ca. 800-500 ka: G1 fan formation and abandonment during a phase of net incision in the upper basin,  
 578 linked to the MPT. No significant geomorphic change recognised in the lower basin. C) ca. 500-110 ka: 100-kyr cycles of  
 579 aggradation and incision recorded by lower basin cut-and-fill terraces (T5, T4, T3). No significant geomorphic change  
 580 recognised in the tributaries of the upper basin. D) From ca. 110 ka: G2 fan formation and abandonment in the upper basin,  
 581 linked to ca. 21/40 kyr climate cycles. Continuation of 100-kyr cycles recorded by lower basin terraces (T2, T1).  
 582

583 To elaborate on the first possibility, the Sierra de Pascha catchments are positioned behind and  
 584 perpendicular to the axis of an elevated northward-plunging anticline (Fig. 2A). In concert with the  
 585 work by Hilley and Strecker (2005), we suggest that channel incision through the resistant anticline  
 586 accelerated sometime between 0.98 and 0.8 Ma. Once this incision propagated upstream and to the east



587 of the anticline, the removal of weakly consolidated sedimentary units in the upper basin was likely  
588 efficient (Hilley and Strecker, 2005). The evolving topography of the anticline could therefore help to  
589 explain the net incision needed in the upper Toro Basin to preserve the alluvial fan surfaces between ca.  
590 800 to 500 ka, and why terrace levels in the lower basin are not recognised during this time interval.

591

592 To elaborate on the second and third possibilities, as late Quaternary glaciations were limited to the  
593 Pascha tributary headwaters (< 5 km from headwall), the hillslope geomorphic response to prolonged  
594 and intensified glaciation may have been very localized (Tofelde et al., 2018). This is apparently true  
595 for the Iglesia and Calingasta Basins in the Western Precordillera where the tributaries, rather than the  
596 main basin record incision following the Mid-Pleistocene Transition (Terrizzano et al., 2017; Peri et al.,  
597 2022). Following this argument, the response time of the Río Toro's long profile to the 100-kyr climate  
598 cycles after the Mid-Pleistocene Transition (ca. 1.2 to 0.8 Ma) may have been substantially longer than  
599 the period of external forcing. If true, this implies that while upstream reaches of the channel may have  
600 experienced no (or a very low amplitude) aggradation/incision cycles (Allen, 2008; McNab et al., 2023).  
601 Alternatively, feedbacks within the system could lead to differences not only in the magnitude of  
602 aggradation/incision, but also the timing. For example, in southwest Peru, Steffan et al. (2009, 2010),  
603 interpreted aggradation in downstream reaches of river channels during past wet climate periods to  
604 result from pulses of sediment mobilized from hillslopes and upstream channel incision.

605

#### 606 *5.2.2 Terrace formation from ca. 500 to 110 ka*

607 From ca. 500 to 110 ka in the upper Toro Basin, we find no record of fan formation (Fig. 8). Curiously  
608 again, though, the lower Toro Basin exhibits a spectacular sequence of terraces showing 100-kyr  
609 cyclicity starting from ca. 500 ka (Tofelde et al., 2017). If long channel response times explain the lack  
610 of terraces from ca. 800 – 500 ka in the lower Toro Basin, to explain the terraces identified in the lower  
611 basin ca. 500 ka (Tofelde et al., 2017), the channel response time must have changed. This could have  
612 occurred as a result of incision in the upper Toro Basin, which would have narrowed the upstream river  
613 valleys, consequently decreasing river response times and enabling aggradation-incision cycles to affect  
614 channel reaches farther downstream (e.g., McNab et al., 2023).

615

616 While a shortened channel response time can explain the formation of terraces in the lower Toro Basin,  
617 it does not explain the absence of terraces/fans in the upper basin over the same period. Consequently,  
618 we next consider other factors that might lead to differences in fan/terrace preservation between the  
619 upper and lower Toro basins.

620

621 Perturbations at the Río Toro outlet, such as a shift in base level, will propagate upstream over time,  
622 thus driving the net incision needed to preserve variations in channel bed elevation in the terrace and  
623 fan sequences. Alternatively, activity along the Gólgota Fault at this time may have adjusted the base



624 level for the trunk stream. Regardless of the exact trigger for base-level fall (e.g., renewed fluvial  
625 connectivity, possibly enhanced by a drop in Lerma Valley lake level) (Malamud et al., 1996; González  
626 Bonorino and Abascal, 2012), a net incisional wave would have propagated upstream from the lower  
627 basin or outlet. That incision would have facilitated terrace preservation in the lower Toro Basin before  
628 the incisional wave propagated upstream to the upper Toro Basin. Steepened reaches of both the trunk  
629 stream and tributaries up to an elevation of ca. 3400 m (Fig. 2C) are consistent with an upstream  
630 propagating wave of incision, which probably only recently reached the ca. 3300-m elevation of the G2  
631 fan toes.

632

633 Consistent with this interpretation, both the upper and lower Toro basins preserve geomorphic evidence  
634 of channel-bed elevation lowering after ca. 100 ka (terraces T2 and T1 in the lower Toro Basin; G2 fan  
635 generation in the upper Toro Basin). Whereas T2 and T1 lie 40 m and 20 m respectively above the  
636 modern Río Toro, the G2 fans are at most 10 m above their closest channel. This finding further supports  
637 the idea that net incision is ongoing in the lower Toro Basin, probably keeping pace with the ongoing  
638 uplift of the Sierra de Pascha Sur (Tofelde et al., 2017), but net incision has possibly only resumed  
639 within the last ca. 110 to 50 kyr in the upper Toro Basin.

640

641 Other factors may have also played a role in the misaligned timing of fan/terrace formation in the upper  
642 and lower Toro basins. Restricted hydrological connectivity or disconnectivity can lead to internal  
643 variability in the nature and timing of a basin's geomorphic or sedimentary response to external  
644 perturbations (Fryirs et al., 2007; Buter et al., 2022). For example, basin connectivity and geometry  
645 appear to have disrupted the timing of climate-driven sediment transfer within the Humahuaca Basin of  
646 NW Argentina during the last glacial cycles, leading to anti-phased timing of aggradation-incision  
647 cycles along tributaries on either side of the valley (Schildgen et al., 2016). No fault lines, which can  
648 influence connectivity (Guarnieri and Pirrotta, 2008; Brocard et al., 2012), intersect the channel network  
649 between the alluvial fans and terrace levels of the Toro Basin (Fig 2) (Pingel et al., 2020). Nevertheless,  
650 minor adjustments to the long profile of an alluvial channel network can be sufficient to affect the  
651 internal connectivity of a basin (Savi et al., 2020). One such adjustment may include the tributary  
652 junction fan at the Quebrada de Chorro outlet, which has created a diffuse knickzone in the Río Toro  
653 long profile (Fig. 2B). As the fan has aggraded, it has pushed the main channel to the opposite valley  
654 side, evidenced by a marked channel bend. The fan may therefore inhibit the coupling between the  
655 upstream and downstream reaches of the trunk stream by disrupting the flow of sediment and (possibly)  
656 water from the Sierra de Pascha tributaries and along the Río Toro (e.g., Harvey 2012). However, the  
657 capacity of the fan to disrupt environmental signals moving through the basin may depend on the  
658 direction of signal travel. For example, channel incision due to a climate-induced increase in water  
659 discharge may continue to propagate downstream, regardless of a new sedimentary input from a major  
660 tributary, unless the tributary fully dams the upstream section. However, if a wave of incision is instead



661 migrating upstream, a tributary junction fan may slow or disrupt its propagation (Savi et al., 2020).  
662 Nevertheless, while sedimentary inputs from individual tributaries can affect the modern channel  
663 profile, and may slow upstream-propagating incisional cycles, it is not clear whether such localized  
664 features will play an important role in channel network evolution over longer (e.g., > 100 kyr)  
665 timescales.

666

### 667 *5.2.3 Fan formation since ca. 110 ka*

668 All G2 surfaces were either stable or actively receiving sediment for some time during both cool, wet  
669 glacial periods and warm, dry interglacials. Similar to the terraces in the lower basin (Tofelde et al.,  
670 2017), the timing of G2 surface abandonment is restricted to glacial phases; enhanced moisture  
671 availability due to an intensified SASM is likely to have amplified sediment transport and channel  
672 incision (Baker and Fritz, 2015). Around the latitude of the Toro Basin, glacial moraine records in the  
673 Central Andes show strong evidence for glacial advances at ca. 16 and 22–24 ka, with some evidence  
674 also for advances at ca. 42 and 55 ka (D’Arcy et al., 2019a; Fig 7B). The stratigraphically highest  
675 surfaces in G2, Qf\_5 and Qf\_6, show abandonment ages that are consistent with the timing of the oldest  
676 glacial advances recorded in the moraine record (ca. 55 ka).

677

678 For surfaces Qf\_7 and Qf\_8, the timing of abandonment is harder to interpret, due to the difficulty in  
679 knowing whether the youngest boulders on each surface are outliers due to erosion/rotation, or if they  
680 represent a time of active deposition on the surface. Given the similarities in surface weathering between  
681 Qf\_6 and Qf\_7, it is possible that Qf\_7 was active at the same time as Qf\_6 and Qf\_5, and hence was  
682 abandoned at a similar time (implying that the youngest boulder of Qf\_7 is an outlier). If the young  
683 boulder instead represents a real depositional age, then the abandonment of Qf\_7 could be linked to the  
684 ca. 22–24 ka glacial advance, coinciding with the northern hemisphere Last Glacial Maximum. The  
685 abandonment of Qf\_8 is similarly challenging to interpret, with abandonment potentially linked to either  
686 the ca. 24 ka glacial advance (associated with the ‘Minchin’ wet climate phase of the Central Andes) if  
687 the youngest boulder is excluded, or the ca. 16 ka glacial advance associated with Heinrich Stadial 1 if  
688 not excluded.

689

690 While we reason that the two youngest ages from Qf\_7 and Qf\_8 are not outliers and instead reflect  
691 later deposition events (see 5.1.2), we have also estimated the timing of surface abandonment without  
692 them (Fig. 7). In this alternative record, the abandonment of three of the four fans fall between ca. 65  
693 and 60 ka. This points to a modest phase of net incision in several Sierra de Pascha catchments during  
694 a wet glacial period (Fritz et al., 2007).

695





696 Overall, the exposure age distributions and estimated abandonment ages appear to capture cycles of fan  
697 aggradation-incision with a periodicity of ca. 20 to 40 kyr. Considering the above tentative links  
698 between abandonment times and glacial advances, and that no known tectonic forcing in the Toro Basin  
699 can explain this cyclicity, the alluvial channel network is likely responding to precession (21-kyr) or  
700 obliquity-driven (40-kyr) climate cycles. Precessional forcing has been recorded within the sedimentary  
701 archives elsewhere in the Central Andes, including fluvial terraces in the Humahuaca Basin (23°S)  
702 (Schildgen et al., 2016) and alluvial fans in the Santa María Basin (26.5°S) (D’Arcy et al., 2018) in NW  
703 Argentina.

704

### 705 **5.3 Impacts of the Mid-Pleistocene Transition on the Toro Basin**

706 The G1 fan surfaces have CRN exposure ages that span several glacial-interglacial cycles (Fig. 6).  
707 Although our interpreted ages are too imprecise to associate with specific glacial phases, 100-kyr glacial  
708 moderation of aggradation-incision cycles is thought to have controlled fluvial terrace formation in the  
709 lower Toro Basin (e.g., Tofelde et al., 2017). In semi-arid landscapes and transport-limited systems, this  
710 finding is not unexpected, as geomorphic activity is invariably amplified during wetter, glacial periods  
711 (Harvey et al., 1999; Spelz et al., 2008; Cesta and Ward, 2016). Given the number of G1 fans (n=4)  
712 capturing the prolonged net incisional phase (>300 kyr), it is possible that eccentricity-driven cycles of  
713 aggradation and incision are also recorded in the upper Toro Basin.

714

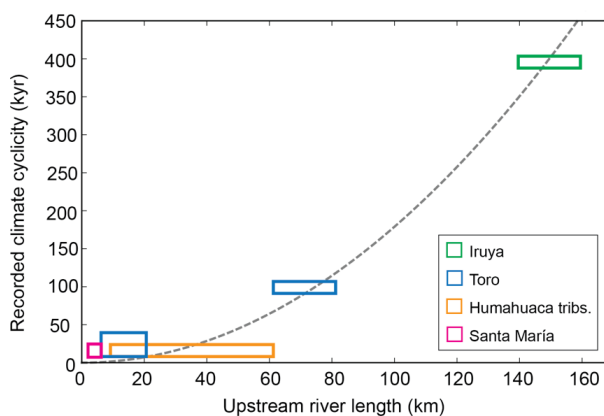
715 Our net incisional phase between ca. 800 and 500 ka coincides with the onset of prolonged and enhanced  
716 global glacial cycles following the Mid-Pleistocene Transition (MPT, 1.2–0.8 Ma) which marked a shift  
717 in climate periodicity from 41 to 100 kyr cycles (Berger et al., 1999). The southward migration of the  
718 ITCZ at this time led to heightened moisture availability throughout the Central Andes (Haselton et al.,  
719 2002; Broccoli et al., 2006; Vizy and Cook, 2007). Alluvial channels in semi-arid regions of the Central  
720 Andes are found to respond quickly to marked shifts in precipitation such as this (e.g., Schildgen et al.,  
721 2016; Tofelde et al., 2017), which also appear to drive phases of enhanced sediment evacuation to the  
722 foreland (Fisher et al., 2023).

723

724 Enhanced incision linked to the MPT has also been recognised at other locations in the Central Andes  
725 (Fig. 1A), including the Casa Grande Basin (23°S) in the Eastern Cordillera, the Salinas Grandes Basin  
726 (23.5°S) of the Puna Plateau (Pingel et al., 2019b), and the Iglesia (30.5°S) and Calingasta (32°S) basins  
727 in the Western Precordillera (Terrizzano et al., 2017; Peri et al., 2022). These observations point to a  
728 regional phase of net incision and therefore landscape response to global climate change. For several of  
729 these locations, including the Toro Basin, local tectonic activity may have provided a secondary driver  
730 for incision, or created conditions conducive to fan/terrace preservation. Towards the Andean interior,  
731 the geomorphic response to the MPT probably lessens, as moisture and the extent of past glaciations is



732 more restricted (Luna et al., 2018; Haselton et al., 2002). Beyond the Central Andes, fluvial terraces  
 733 along the Río Deseado (47°S) (Tobal et al., 2021) and Río Santa Cruz (50°S) (Milanez Fernandes,  
 734 2023), draining the Southern Andes in Patagonia also record a period of net incision that can be  
 735 tentatively linked to the MPT. On a global scale, a growing number of studies have identified periods  
 736 of intensified erosion at this time, for example in the St. Elias mountains, Alaska (Gulick et al., 2015),  
 737 Central Appalachia (Del Vecchio et al., 2022), the Rocky Mountains (Pederson and Egholm, 2013) and  
 738 the European Alps (Haeuselmann et al., 2007; Valla et al., 2011; Sternai et al., 2013). While it is not  
 739 possible to discount a tectonic influence on landscape change in the upper Toro basin entirely, the links  
 740 between MPT climate and incision, and its expression elsewhere in the Andes and beyond, is  
 741 compelling.  
 742



743

744 **Figure 9.** Correlation between recorded climate cyclicity and upstream river length recognised in four basins of the Central  
 745 Andes (Fisher et al., 2016; Schildgen et al., 2016; Tofelde et al., 2017; D’Arcy et al. 2018; this study). Adapted from Tofelde  
 746 et al. (2017). Recorded period:  $0.019 \times \text{river length}^2$ .

747

#### 748 5.4 Climate periodicity and alluvial channel system length

749 Higher frequency climate cycles are recorded in fan generation G2 of the Sierra de Pascha tributaries  
 750 compared with the mainstem of the basin; the alluvial fans, which appear to record climate cycles with  
 751 a periodicity of ca. 20 to 40-kyr have an upstream channel length of ~10 km and are positioned ~30 km  
 752 upstream of the terrace sequence showing 100-kyr climate cyclicity dated by Tofelde et al. (2017). This  
 753 finding substantiates the theory that the response time of alluvial channel systems to perturbations in  
 754 climate depends on system length (Paola et al., 1992; Castellort and Van Den Driessche, 2003; Godard  
 755 et al., 2013; McNab et al., 2023). Evidence of this relationship, together with the dependency on the  
 756 square of the system length, was identified in the archive of several sedimentary basins in the Central  
 757 Andes, although only a single forcing frequency was recorded within each basin (Fig. 9) (Tofelde et al.,  
 758 2017). Our new data from the Toro Basin provide critical field evidence that multiple climate



759 periodicities can be preserved within the sedimentary record of a single sedimentary basin, with higher  
760 forcing frequencies recorded only in the uppermost reaches of the basin.

761

## 762 **6. Conclusions**

763

764 The alluvial fan and terrace sequences of the Toro basin present an excellent opportunity to explore (1)  
765 how channel responses to external perturbations may or may not propagate downstream, and (2) the  
766 differences in landscape response to forcing frequency as a function of stream length. We applied CRN  
767 dating to a suite of alluvial fan surfaces to characterise the evolution of the alluvial channel network of  
768 the Toro basin over the last one million years. Our key findings are as follows:

769

770 1. We identified two generations of fan surfaces (G1 and G2) were identified in the Sierra de  
771 Pascha tributary catchments. The G1 fans record CRN exposure ( $^{10}\text{Be}$ ) ages between ca. 800  
772 and 500 ka, whereas the G2 fans record surface activity and then abandonment between ca. 100  
773 and 20 ka.

774 2. The G1 fans capture a significant phase of net incision (~ 200 m) between ca. 800 and 500 ka.  
775 The stepwise evacuation of the upper basin coincides with the onset of prolonged and enhanced  
776 global glacial cycles following the Mid-Pleistocene Transition (MPT). With several basins in  
777 the Central Andes and beyond also registering this phase of incision, we propose that the G1  
778 fans are part of a continental scale response to MPT climate change.

779 3. The abandonment of the G2 fans is restricted to glacial periods, mostly modulated by 21/40-  
780 kyr climate cycles; enhanced moisture availability due to an intensified SASM likely amplified  
781 channel incision and sediment transport.

782 4. Differences in the timing of alluvial fan and fluvial terrace development in the upper and lower  
783 Toro basins appear to be associated with how channel length affects fluvial response time to  
784 climate forcing as well as local controls on net incision, which facilitates preservation of the  
785 geomorphic record of aggradation-incision cycles.

786 5. The new alluvial fan record from the upper Toro Basin, combined with earlier results on fluvial  
787 terraces from the lower Toro Basin, provides field evidence for the theoretical predictions of a  
788 scaling relationship between climate forcing frequency recorded in sedimentary archives and  
789 the system length. We show that multiple climate periodicities can be preserved within the  
790 sedimentary record of a single sedimentary basin, with higher forcing frequencies recorded only  
791 in the uppermost reaches of the basin. This improved understanding of the role of system length  
792 in climate signal propagation is an important step forward in helping us to anticipate the spatial  
793 distribution of sedimentary paleoclimate records within landscapes.

794

795



796 **7. Code/data availability**

797 All data is included as part of the manuscript.

798

799 **8. Author contribution**

800 Conceptualization: E.N.O, T.F.S, S.T; Sample collection and processing: E.N.O, T.F.S, S.T, H.W.;

801 Visualization: E.N.O with feedback from all authors; Writing & editing: all authors.

802

803 **9. Competing interests**

804 The authors declare that they have no conflict of interest.

805

806 **10. Acknowledgments**

807 This work was co-funded by (1) the German Research Foundation (DFG) grant 373/34-1 and the  
808 Brandenburg Ministry of Sciences, Research, and Cultural Affairs, within the framework of the  
809 International Research Training Group IGK2018 SuRfAce processes, TEctonics and Georesources: The  
810 Andean foreland basin of Argentina (StRATEGy) and (2) the European Research Council (ERC) under  
811 the European Union's Horizon 2020 Research and Innovation program (ERC Consolidator Grant  
812 863490 to T.F.S.). TanDEM-X 12-m resolution digital elevation data were provided by the German  
813 Aerospace Center (DLR) through grant DEM\_GEOL1915 to T.F. S. We thank Yanina Rojo for logistical  
814 support leading up to and during all field work. We also thank Peter van der Beek for assistance during  
815 field work.

816

817 **11. References**

818

- 819 Armitage, J.J., Dunkley Jones, T., Duller, R.A., Whittaker, A.C., Allen, P.A. Temporal buffering of  
820 climate-driven sediment flux cycles by transient catchment response. *Earth and Planetary  
821 Science Letters*, 369–370, 200–210. <https://doi.org/10.1016/j.epsl.2013.03.020>, 2013.
- 822 Baker, P.A., Rigsby, C.A., Seltzer, G.O., Fritz, S.C., Lowenstein, T.K., Bacher, N.P., Veliz, C. Tropical  
823 climate changes at millennial and orbital timescales on the Bolivian Altiplano. *Nature*,  
824 409(6821), 698–701. <https://doi.org/10.1038/35055524>, 2001.
- 825 Baker, P.A., Fritz, S.C. Nature and causes of Quaternary climate variation of tropical South America.  
826 *Quaternary Science Reviews*., 124, 31–47. <https://doi.org/10.1016/j.quascirev.2015.06.011>,  
827 2015.
- 828 Berger, A., Li, X.S., Loutre, M.F. Modelling northern hemisphere ice volume over the last 3 Ma.  
829 *Quaternary Science Reviews*, 18(1), 1–11. [https://doi.org/10.1016/S0277-3791\(98\)00033-X](https://doi.org/10.1016/S0277-3791(98)00033-X),  
830 1999.
- 831 Berger, A., Loutre, M.F. Insolation values for the climate of the last 10 million years. *Quaternary  
832 Science Reviews*, 10(4), 297–317. [https://doi.org/10.1016/0277-3791\(91\)90033-Q](https://doi.org/10.1016/0277-3791(91)90033-Q), 1991.
- 833 Bernard, T., Sinclair, H.D., Gailleton, B., Mudd, S.M., Ford, M. Lithological control on the post-  
834 orogenic topography and erosion history of the Pyrenees. *Earth and Planetary Science Letters*,  
835 518, 53–66. <https://doi.org/10.1016/j.epsl.2019.04.034>, 2019.
- 836 Blard, P.-H., Braucher, R., Lavé, J., Bourlès, D. Cosmogenic <sup>10</sup>Be production rate calibrated against  
837 <sup>3</sup>He in the high Tropical Andes (3800–4900 m, 20–22° S). *Earth and Planetary Science Letters*,  
838 382, 140–149. <https://doi.org/10.1016/j.epsl.2013.09.010>, 2013.
- 839 Bobst, A.L., Lowenstein, T.K., Jordan, T.E., Godfrey, L.V., Ku, T.L., Luo, S. A 106 ka paleoclimate  
840 record from drill core of the Salar de Atacama, northern Chile. *Palaeogeography,  
841 Palaeoclimatology, Palaeoecology*, 173(1–2), 21–42. [https://doi.org/10.1016/S0031-  
842 0182\(01\)00308-X](https://doi.org/10.1016/S0031-0182(01)00308-X), 2001.
- 843 Bonorino, G.G., Abascal, L. Drainage and base-level adjustments during evolution of a late Pleistocene  
844 piggyback basin, Eastern Cordillera, Central Andes of northwestern Argentina. *Bulletin*,  
845 124(11–12), 1858–1870. <https://doi.org/10.1130/B30395.1>, 2012.
- 846 Bookhagen, B., Strecker, M.R. Orographic barriers, high-resolution TRMM rainfall, and relief  
847 variations along the eastern Andes. *Geophysical Research Letters*, 35.  
848 <https://doi.org/10.1029/2007GL032011>, 2008.



- 849 Brocard, G., Willenbring, J., Suski, B., Audra, P., Authemayou, C., Cosenza-Murales, B., Morán-Ical,  
850 S., Demory, F., Rochette, P., Vennemann, T., Holliger, K. Rate and processes of river network  
851 rearrangement during incipient faulting: The case of the Cahabón River, Guatemala. *American*  
852 *Journal of Science*, 312(5), 449-507, <https://doi.org/10.2475/05.2012.01>, 2012.
- 853 Broccoli, A.J., Dahl, K.A., Stouffer, R.J. Response of the ITCZ to Northern Hemisphere cooling.  
854 *Geophysical Research Letters*, 33(1). <https://doi.org/10.1029/2005GL024546>, 2006.
- 855 Brooke, S.A., Whittaker, A.C., Armitage, J.J., D'Arcy, M., Watkins, S.E. Quantifying sediment  
856 transport dynamics on alluvial fans from spatial and temporal changes in grain size, Death  
857 Valley, California. *Journal of Geophysical Research: Earth Surface*, 123(8), 2039-2067.  
858 <https://doi.org/10.1029/2018JF004622>, 2018.
- 859 Bufo, A., Burbank, D.W., Liu, L., Bookhagen, B., Qin, J., Chen, J., Li, T., Thompson Jobe, J.A., Yang,  
860 H. Variations of lateral bedrock erosion rates control planation of uplifting folds in the foreland  
861 of the Tian Shan, NW China. *Journal of Geophysical Research: Earth Surface*, 122(12), 2431-  
862 2467. <https://doi.org/10.1002/2016JF004099>, 2017.
- 863 Buter, A., Heckmann, T., Filisetti, L., Savi, S., Mao, L., Gems, B., Comiti, F. Effects of catchment  
864 characteristics and hydro-meteorological scenarios on sediment connectivity in glacierised  
865 catchments. *Geomorphology*, 402, 108128. <https://doi.org/10.1016/j.geomorph.2022.108128>,  
866 2022.
- 867 Castellort, S., Van Den Driessche, J. How plausible are high-frequency sediment supply-driven cycles  
868 in the stratigraphic record? *Sedimentary Geology*, 157, 3–13. [https://doi.org/10.1016/S0037-  
869 0738\(03\)00066-6](https://doi.org/10.1016/S0037-0738(03)00066-6), 2003.
- 870 Castino, F., Bookhagen, B., Strecker, M.R. Rainfall variability and trends of the past six decades (1950–  
871 2014) in the subtropical NW Argentine Andes. *Climate Dynamics*, 48, 1049-1067.  
872 <https://doi.org/10.1007/s00382-016-3127-2>, 2017.
- 873 Cesta, J.M., Ward, D.J. Timing and nature of alluvial fan development along the Chajnantor Plateau,  
874 northern Chile. *Geomorphology*, 273, 412–427.  
875 <https://doi.org/10.1016/j.geomorph.2016.09.003>, 2016.
- 876 Clarke, L., Quine, T.A., Nicholas, A. An experimental investigation of autogenic behaviour during  
877 alluvial fan evolution. *Geomorphology*, 115(3-4), 278-285.  
878 <https://doi.org/10.1016/j.geomorph.2009.06.033>, 2010.
- 879 Counts, R.C., Murari, M.K., Owen, L.A., Mahan, S.A., Greenan, M. Late Quaternary  
880 chronostratigraphic framework of terraces and alluvium along the lower Ohio River,  
881 southwestern Indiana and western Kentucky, USA. *Quaternary Science Reviews*, 110, 72-91.  
882 <https://doi.org/10.1016/j.quascirev.2014.11.011>, 2015.
- 883 Crivellari, S., Chiessi, C.M., Kuhnert, H., Häggi, C., da Costa Portilho-Ramos, R., Zeng, J.Y., Zhang,  
884 Y., Schefuß, E., Mollenhauer, G., Hefter, J., Alexandre, F. Increased Amazon freshwater  
885 discharge during late Heinrich Stadial 1. *Quaternary Science Reviews*, 181, 144-155.  
886 <https://doi.org/10.1016/j.quascirev.2017.12.005>, 2018.
- 887 D'Arcy, M.K., Schildgen, T.F., Strecker, M.R., Wittmann, H., Duesing, W., Mey, J., Tofelde, S.,  
888 Weissmann, P., Alonso, R.N. Timing of past glaciation at the Sierra de Aconquija, northwestern  
889 Argentina, and throughout the Central Andes. *Quaternary Science Reviews*, 204, 37–57.  
890 <https://doi.org/10.1016/j.quascirev.2018.11.022>, 2019a.
- 891 D'Arcy, M.K., Schildgen, T.F., Turowski, J.M., Dinezio, P. Inferring the timing of abandonment of  
892 aggraded alluvial surfaces dated with cosmogenic nuclides. *Earth Surface Dynamics*, 7, 755–  
893 771. <https://doi.org/10.5194/esurf-7-755-2019>, 2019b.
- 894 D'Arcy, M., Schildgen, T.F., Tofelde, S., Strecker, M.R., Wittmann, H., Düsing, W., Weissmann, P.  
895 and Roda-Boluda, D.C. Catchment-alluvial fan systems record > 200 ka of millennial-scale  
896 climate changes in the subtropical Andes. *EGU General Assembly Conference Abstracts*.  
897 <https://ui.adsabs.harvard.edu/abs/2018EGUGA..20.4710D/abstract>, 2018.
- 898 DeCelles, P.G., Carrapa, B., Horton, B.K., Gehrels, G.E. Cenozoic foreland basin system in the central  
899 Andes of northwestern Argentina: Implications for Andean geodynamics and modes of  
900 deformation. *Tectonics*, 30(6). <https://doi.org/10.1029/2011TC002948>, 2011.
- 901 Del Vecchio, J., DiBiase, R.A., Corbett, L.B., Bierman, P.R., Caffee, M.W., Ivory, S.J. Increased  
902 erosion rates following the onset of Pleistocene periglaciation at Bear Meadows, Pennsylvania,



- 903 USA. *Geophysical Research Letters*, 49(4), p.e2021GL096739.  
904 <https://doi.org/10.1029/2021GL096739>, 2022.
- 905 Dey, S., Thiede, R.C., Schildgen, T.F., Wittmann, H., Bookhagen, B., Scherler, D., Jain, V., Strecker,  
906 M.R. Climate-driven sediment aggradation and incision since the late Pleistocene in the NW  
907 Himalaya, India. *Earth and Planetary Science Letters*, 449, 321–331.  
908 <https://doi.org/10.1016/j.epsl.2016.05.050>, 2016.
- 909 Dortch, J.M., Tomkins, M.D., Saha, S., Murari, M.K., Schoenbohm, L.M., Curl, D. A tool for the ages:  
910 The Probabilistic Cosmogenic Age Analysis Tool (P-CAAT). *Quaternary Geochronology*, 71,  
911 101323. <https://doi.org/10.1016/j.quageo.2022.101323>, 2022.
- 912 Dühnforth, M., Densmore, A.L., Ivy-Ochs, S., Allen, P., Kubik, P.W. Early to Late Pleistocene history  
913 of debris-flow fan evolution in western Death Valley (California) using cosmogenic  $^{10}\text{Be}$  and  
914  $^{26}\text{Al}$ . *Geomorphology*, 281, 53–65. <https://doi.org/10.1016/j.geomorph.2016.12.020>, 2017.
- 915 Dühnforth, M., Densmore, A.L., Ivy-Ochs, S., Allen, P.A., Kubik, P.W. Timing and patterns of debris  
916 flow deposition on Shepherd and Symmes creek fans, Owens Valley, California, deduced from  
917 cosmogenic  $^{10}\text{Be}$ . *Journal of Geophysical Research: Earth Surface*, 112.  
918 <https://doi.org/10.1029/2006JF000562>, 2007.
- 919 Dunai, T.J., López, G.A.G., Juez-Larré, J. Oligocene–Miocene age of aridity in the Atacama Desert  
920 revealed by exposure dating of erosion-sensitive landforms. *Geology*, 33(4), 321–324.  
921 <https://doi.org/10.1130/G21184.1>, 2005.
- 922 Fernandes, V.M., Schildgen, T., Ruby, A., Wittmann-Oelze, H., McNab, F. Pleistocene Landscape  
923 Evolution in Southern Patagonia: A Record of Regional Incision from  $^{10}\text{Be}$  Dating of Fluvial  
924 Terraces (No. EGU23-15938). Copernicus Meetings. [https://doi.org/10.5194/egusphere-  
925 egu23-15938](https://doi.org/10.5194/egusphere-egu23-15938), 2023.
- 926 Fisher, G.B., Luna, L.V., Amidon, W.H., Burbank, D.W., de Boer, B., Stap, L.B., Bookhagen, B.,  
927 Godard, V., Oskin, M.E., Alonso, R.N., and Tuenter, E. Milankovitch-paced erosion in the  
928 southern Central Andes. *Nature Communications*, 14(1), 424 [https://doi.org/10.1038/s41467-  
929 023-36022-0](https://doi.org/10.1038/s41467-023-36022-0), 2023.
- 930 Fritz, S.C., Baker, P.A., Ekdahl, E., Seltzer, G.O., Stevens, L.R. Millennial-scale climate variability  
931 during the Last Glacial period in the tropical Andes. *Quaternary Science Reviews*, 29(7-8),  
932 1017–1024. <https://doi.org/10.1016/j.quascirev.2010.01.001>, 2010.
- 933 Fritz, S.C., Baker, P.A., Seltzer, G.O., Ballantyne, A., Tapia, P., Cheng, H., Edwards, R.L. Quaternary  
934 glaciation and hydrologic variation in the South American tropics as reconstructed from the  
935 Lake Titicaca drilling project. *Quaternary Research*, 68(3), 410–420.  
936 <https://doi.org/10.1016/j.yqres.2007.07.008>, 2007.
- 937 Fritz, S.C., Baker, P.A., Lowenstein, T.K., Seltzer, G.O., Rigsby, C.A., Dwyer, G.S., Tapia, P.M.,  
938 Arnold, K.K., Ku, T.L., Luo, S. Hydrologic variation during the last 170,000 years in the  
939 southern hemisphere tropics of South America. *Quaternary Research*, 61(1), 95–104.  
940 <https://doi.org/10.1016/j.yqres.2003.08.007>, 2004.
- 941 Fryirs, K.A., Brierley, G.J., Preston, N.J., Kasai, M. Buffers, barriers and blankets: The (dis)  
942 connectivity of catchment-scale sediment cascades. *Catena*, 70(1), 49–67.  
943 <https://doi.org/10.1016/j.catena.2006.07.007>, 2007.
- 944 Ganev, P.N., Dolan, J.F., Frankel, K.L., Finkel, R.C. Rates of extension along the Fish Lake Valley  
945 fault and transtensional deformation in the Eastern California shear zone–Walker Lane belt.  
946 *Lithosphere*, 2(1), 33–49. <https://doi.org/10.1130/L51.1>, 2010.
- 947 García, V.H., Hongn, F., Cristallini, E.O. Late Miocene to recent morphotectonic evolution and  
948 potential seismic hazard of the northern Lerma valley: clues from Lomas de Medeiros,  
949 Cordillera Oriental, NW Argentina. *Tectonophysics*, 608, 1238–1253.  
950 <https://doi.org/10.1016/j.tecto.2013.06.021>, 2013.
- 951 Godard, V., Tucker, G.E., Burch Fisher, G., Burbank, D.W., Bookhagen, B. Frequency-dependent  
952 landscape response to climatic forcing. *Geophysical Research Letters*, 40, 859–863.  
953 <https://doi.org/10.1002/grl.50253>, 2013.
- 954 Godfrey, L.V., Jordan, T.E., Lowenstein, T.K., Alonso, R.L. Stable isotope constraints on the transport  
955 of water to the Andes between 22 and 26 S during the last glacial cycle. *Palaeogeography,  
956 Palaeoclimatology, Palaeoecology*, 194(1-3), 299–317. [https://doi.org/10.1016/S0031-  
957 0182\(03\)00283-9](https://doi.org/10.1016/S0031-0182(03)00283-9), 2003.





- 1958 Gosling, W.D., Bush, M.B., Hanselman, J.A., Chepstow-Lusty, A. Glacial-interglacial changes in  
1959 moisture balance and the impact on vegetation in the southern hemisphere tropical Andes  
1960 (Bolivia/Peru). *Palaeogeography, Palaeoclimatology, Palaeoecology*, 259(1), 35-50.  
1961 <https://doi.org/10.1016/j.palaeo.2007.02.050>, 2008.
- 1962 Gray, H.J., Owen, L.A., Dietsch, C., Beck, R.A., Caffee, M.A., Finkel, R.C., Mahan, S.A. Quaternary  
1963 landscape development, alluvial fan chronology and erosion of the Mecca Hills at the southern  
1964 end of the San Andreas fault zone. *Quaternary Science Reviews*, 105, 66-85.  
1965 <https://doi.org/10.1016/j.quascirev.2014.09.009>, 2014.
- 1966 Guarnieri, P., Pirrotta, C. The response of drainage basins to the late Quaternary tectonics in the Sicilian  
1967 side of the Messina Strait (NE Sicily). *Geomorphology*, 95(3-4), 260-273.  
1968 <https://doi.org/10.1016/j.geomorph.2007.06.013>, 2008.
- 1969 Gulick, S.P., Jaeger, J.M., Mix, A.C., Asahi, H., Bahlburg, H., Belanger, C.L., Berbel, G.B., Childress,  
1970 L., Cowan, E., Drab, L., Forwick, M. Mid-Pleistocene climate transition drives net mass loss  
1971 from rapidly uplifting St. Elias Mountains, Alaska. *Proceedings of the National Academy of  
1972 Sciences*, 112(49), 15042-15047. <https://doi.org/10.1073/pnas.1512549112>, 2015.
- 1973 Haeuselmann, P., Granger, D.E., Jeannin, P.Y., Lauritzen, S.E. Abrupt glacial valley incision at 0.8 Ma  
1974 dated from cave deposits in Switzerland. *Geology*, 35(2), 143-146.  
1975 <https://doi.org/10.1130/G23094A>, 2007.
- 1976 Hain, M.P., Strecker, M.R., Bookhagen, B., Alonso, R.N., Pingel, H., Schmitt, A.K. Neogene to  
1977 Quaternary broken foreland formation and sedimentation dynamics in the Andes of NW  
1978 Argentina (25 S). *Tectonics*, 30(2). <https://doi.org/10.1029/2010TC002703>, 2011.
- 1979 Harvey, A.M. The coupling status of alluvial fans and debris cones: a review and synthesis. *Earth  
1980 Surface Processes and Landforms*, 37(1), 64-76. <https://doi.org/10.1002/esp.2213>, 2012.
- 1981 Harvey, A.M., Silva, P.G., Mather, A.E., Goy, J.L., Stokes, M., Zazo, C. The impact of Quaternary sea-  
1982 level and climatic change on coastal alluvial fans in the Cabo de Gata ranges, southeast Spain.  
1983 *Geomorphology*, 28(1-2), 1-22 [https://doi.org/10.1016/S0169-555X\(98\)00100-7](https://doi.org/10.1016/S0169-555X(98)00100-7), 1999.
- 1984 Haselton, K., Hilley, G., Strecker, M.R. Average Pleistocene climatic patterns in the southern central  
1985 Andes: Controls on mountain glaciation and paleoclimate implications. *The Journal of  
1986 Geology*, 110(2), 211-226. 2002.
- 1987 Hedrick, K., Owen, L.A., Rockwell, T.K., Meigs, A., Costa, C., Caffee, M.W., Masana, E., Ahumada,  
1988 E. Timing and nature of alluvial fan and strath terrace formation in the Eastern Precordillera of  
1989 Argentina. *Quaternary Science Reviews*, 80, 143-168  
1990 <https://doi.org/10.1016/j.quascirev.2013.05.004>, 2013.
- 1991 Hidy, A.J., Gosse, J.C., Pederson, J.L., Mattern, J.P., Finkel, R.C. A geologically constrained Monte  
1992 Carlo approach to modeling exposure ages from profiles of cosmogenic nuclides: An example  
1993 from Lees Ferry, Arizona. *Geochemistry Geophysics Geosystems*, 11, Q0AA10.  
1994 <https://doi.org/10.1029/2010GC003084>, 2010.
- 1995 Hilley, G.E., Strecker, M.R. Processes of oscillatory basin filling and excavation in a tectonically active  
1996 orogen: Quebrada del Toro Basin, NW Argentina. *Bulletin of the Geological Society of  
1997 America*, 117, 887-901. <https://doi.org/10.1130/B25602.1>, 2005.
- 1998 Howard, A.D. Equilibrium and time scales in geomorphology: Application to sand-bed alluvial streams.  
1999 *Earth Surface Processes and Landforms*, 7(4), pp.303-325.  
1000 <https://doi.org/10.1002/esp.3290070403>, 1982.
- 1001 Hughes, P.D. Geomorphology and Quaternary stratigraphy: The roles of morpho-, litho-, and  
1002 allostratigraphy. *Geomorphology*, 123, 189-199.  
1003 <https://doi.org/10.1016/j.geomorph.2010.07.025>, 2010.
- 1004 Imbrie, John., McIntyre, Andrew. SST vs time for core V25-21 (specmap.059). PANGAEA., 2006.
- 1005 Kelly, M.A., Lowell, T. V., Applegate, P.J., Phillips, F.M., Schaefer, J.M., Smith, C.A., Kim, H.,  
1006 Leonard, K.C., Hudson, A.M. A locally calibrated, late glacial <sup>10</sup>Be production rate from a low-  
1007 latitude, high-altitude site in the Peruvian Andes. *Quaternary Geochronology*, 26, 70-85.  
1008 <https://doi.org/10.1016/j.quageo.2013.10.007>, 2015.
- 1009 Kleinert, K., Strecker, M.R. Climate change in response to orographic barrier uplift: Paleosol and stable  
1010 isotope evidence from the late Neogene Santa Maria basin, northwestern Argentina. *Geological  
1011 Society of America Bulletin*, 113(6), 728-742. [https://doi.org/10.1130/0016-7606\(2001\)113<0728:CCIRTO>2.0.CO;2](https://doi.org/10.1130/0016-7606(2001)113<0728:CCIRTO>2.0.CO;2), 2001.
- 1012





- 1013 Kober, F., Zeilinger, G., Ivy-Ochs, S., Dolati, A., Smit, J., Kubik, P.W. Climatic and tectonic control  
1014 on fluvial and alluvial fan sequence formation in the Central Makran Range, SE-Iran. *Global*  
1015 *and Planetary Change*, 111, 133-149. <https://doi.org/10.1016/j.gloplacha.2013.09.003>, 2013.
- 1016 Lal, D. Cosmic ray labeling of erosion surfaces: in situ nuclide production rates and erosion models.  
1017 *Earth and Planetary Science Letters*, 104, 424–439. [https://doi.org/10.1016/0012-](https://doi.org/10.1016/0012-821X(91)90220-C)  
1018 [821X\(91\)90220-C](https://doi.org/10.1016/0012-821X(91)90220-C), 1991.
- 1019 Lifton, N., Sato, T., Dunai, T.J. Scaling in situ cosmogenic nuclide production rates using analytical  
1020 approximations to atmospheric cosmic-ray fluxes. *Earth and Planetary Science Letters*, 386,  
1021 149–160. <https://doi.org/10.1016/j.epsl.2013.10.052>, 2014.
- 1022 Lisiecki, L.E., Raymo, M.E. Diachronous benthic  $\delta^{18}\text{O}$  responses during late Pleistocene terminations.  
1023 *Paleoceanography*, 24(3). <https://doi.org/10.1029/2009PA001732>, 2009.
- 1024 Luna, L. V., Bookhagen, B., Niedermann, S., Rugel, G., Scharf, A., Merchel, S. Glacial chronology and  
1025 production rate cross-calibration of five cosmogenic nuclide and mineral systems from the  
1026 southern Central Andean Plateau. *Earth and Planetary Science Letters*, 500, 242–253.  
1027 <https://doi.org/10.1016/j.epsl.2018.07.034>, 2018.
- 1028 Ma, Y., Stuart, F.M. The use of in-situ cosmogenic  $^{21}\text{Ne}$  in studies on long-term landscape development.  
1029 *Acta Geochimica*, 37, 310-322. <https://doi.org/10.1007/s11631-017-0216-9>, 2018.
- 1030 Mackin, J. Concept of the graded river. *Geological Society of America Bulletin*, 59(5), 463-512, 1948.
- 1031 Malamud, B.D., Jordan, T.E., Alonso, R.A., Gallardo, E.F., Gonzalez, R.E., Kelley, S.A. Pleistocene  
1032 Lake Lerma, Salta Province, NW Argentina. In XIII Congreso Geológico Argentino y III  
1033 Congreso de Exploración de Hidrocarburos, Vol. 1, 103-114, 1996.
- 1034 Marrett, R., Strecker, M.R. Response of intracontinental deformation in the central Andes to late  
1035 Cenozoic reorganization of South American Plate motions. *Tectonics*, 19(3), 452-467.  
1036 <https://doi.org/10.1029/1999TC001102>, 2000.
- 1037 Marrett, R.A., Allmendinger, R.W., Alonso, R.N., Drake, R.E. Late Cenozoic tectonic evolution of the  
1038 Puna Plateau and adjacent foreland, northwestern Argentine Andes. *Journal of South American*  
1039 *Earth Sciences*, 7(2), 179-207. [https://doi.org/10.1016/0895-9811\(94\)90007-8](https://doi.org/10.1016/0895-9811(94)90007-8), 1994.
- 1040 Martin, L.C.P., Blard, P.-H., Balco, G., Lavé, J., Delunel, R., Lifton, N., Laurent, V. The CREp program  
1041 and the ICE-D production rate calibration database: A fully parameterizable and updated online  
1042 tool to compute cosmic-ray exposure ages. *Quaternary Geochronology*, 38, 25–49.  
1043 <https://doi.org/10.1016/j.quageo.2016.11.006>, 2017.
- 1044 Martin, L.C.P., Blard, P.-H., Lavé, J., Braucher, R., Lupker, M., Condom, T., Charreau, J., Mariotti, V.,  
1045 ASTER Team, Davy, E. In situ cosmogenic  $^{10}\text{Be}$  production rate in the High Tropical Andes.  
1046 *Quaternary Geochronology*, 30, 54–68. <https://doi.org/10.1016/j.quageo.2015.06.012>, 2015.
- 1047 Martin, L.C., Blard, P.H., Lavé, J., Condom, T., Prémaillon, M., Jomelli, V., Brunstein, D., Lupker, M.,  
1048 Charreau, J., Mariotti, V., Tibari, B. Lake Tauca highstand (Heinrich Stadial 1a) driven by a  
1049 southward shift of the Bolivian High. *Science Advances*, 4(8),  
1050 <https://doi.org/10.1126/sciadv.aar2514>, 2018.
- 1051 Martini, M.A., Kaplan, M.R., Strelin, J.A., Astini, R.A., Schaefer, J.M., Caffee, M.W., Schwartz, R.  
1052 Late Pleistocene glacial fluctuations in Cordillera oriental, subtropical Andes. *Quaternary*  
1053 *Science Reviews*, 171, 245-259. <https://doi.org/10.1016/j.quascirev.2017.06.033>, 2017.
- 1054 Mather, A.E., Stokes, M., Whitfield, E. River terraces and alluvial fans: The case for an integrated  
1055 Quaternary fluvial archive. *Quaternary Science Reviews* 166, 74-90,  
1056 <https://doi.org/10.1016/j.quascirev.2016.09.022>, 2017.
- 1057 Mazzuoli, R., Vezzoli, L., Omarini, R., Acocella, V., Gioncada, A., Matteini, M., Dini, A., Guillou, H.,  
1058 Hauser, N., Uttini, A., Scaillet, S. Miocene magmatism and tectonics of the easternmost sector  
1059 of the Calama–Olacapato–El Toro fault system in Central Andes at ~ 24 S: Insights into the  
1060 evolution of the Eastern Cordillera. *GSA Bulletin* 120(11-12), 1493-1517,  
1061 <https://doi.org/10.1130/B26109.1>, 2008.
- 1062 McFadden, L.D., Ritter, J.B., Wells, S.G. Use of Multiparameter Relative-Age Methods for Age  
1063 Estimation and Correlation of Alluvial Fan Surfaces on a Desert Piedmont, Eastern Mojave  
1064 Desert, California. *Quaternary Research* 32, 276–290, [https://doi.org/10.1016/0033-](https://doi.org/10.1016/0033-5894(89)90094-X)  
1065 [5894\(89\)90094-X](https://doi.org/10.1016/0033-5894(89)90094-X), 1989.



- 1066 McNab, F., Schildgen, T.F., Turowski, J.M., Wickert, A.D. Diverse responses of alluvial rivers to  
1067 periodic environmental change. *Geophysical Research Letters* 50(10), e2023GL103075,  
1068 <https://doi.org/10.1029/2023GL103075>, 2023.
- 1069 Mescolotti, P.C., do Nascimento Pupim, F., Ladeira, F.S.B., Sawakuchi, A.O., Santa Catharina, A.,  
1070 Assine, M.L. Fluvial aggradation and incision in the Brazilian tropical semi-arid: Climate-  
1071 controlled landscape evolution of the São Francisco River. *Quaternary Science Reviews* 263,  
1072 106977, <https://doi.org/10.1016/j.quascirev.2021.106977>, 2021.
- 1073 Mey, J., D'Arcy, M.K., Schildgen, T.F., Egholm, D.L., Wittmann, H., Strecker, M.R. Temperature and  
1074 precipitation in the southern Central Andes during the last glacial maximum, Heinrich Stadial  
1075 1, and the Younger Dryas. *Quaternary Science Reviews* 248, 106592,  
1076 <https://doi.org/10.1016/j.quascirev.2020.106592>, 2020.
- 1077 Mosblech, N.A., Bush, M.B., Gosling, W.D., Hodell, D., Thomas, L., Van Calsteren, P., Correa-Metrio,  
1078 A., Valencia, B.G., Curtis, J., Van Woeseik, R. North Atlantic forcing of Amazonian  
1079 precipitation during the last ice age. *Nature Geoscience* 5(11), 817-820,  
1080 <https://doi.org/10.1038/ngeo1588>, 2012.
- 1081 Mouchéné, M., van der Beek, P., Carretier, S., Mouthereau, F. Autogenic versus allogenic controls on  
1082 the evolution of a coupled fluvial megafan–mountainous catchment system: numerical  
1083 modelling and comparison with the Lannemezan megafan system (northern Pyrenees, France).  
1084 *Earth Surface Dynamics* 5(1), 125-143, <https://doi.org/10.5194/esurf-5-125-2017>, 2017.
- 1085 Mouslopoulou, V., Begg, J., Fülling, A., Moraetis, D., Partsinevelos, P., Oncken, O. Distinct phases of  
1086 eustatic and tectonic forcing for late Quaternary landscape evolution in southwest Crete,  
1087 Greece. *Earth Surface Dynamics* 5(3), 511-527, <https://doi.org/10.5194/esurf-5-511-2017>,  
1088 2017.
- 1089 Nicholas, A.P., Quine, T.A. Modeling alluvial landform change in the absence of external  
1090 environmental forcing. *Geology* 35(6), 527-530, <https://doi.org/10.1130/G23377A.1>, 2007.
- 1091 Nishiizumi, K., Winterer, E.L., Kohl, C.P., Klein, J., Middleton, R., Lal, D., Arnold, J.R. Cosmic ray  
1092 production rates of  $^{10}\text{Be}$  and  $^{26}\text{Al}$  in quartz from glacially polished rocks. *Journal of Geophysical*  
1093 *Research* 94, 17907, <https://doi.org/10.1029/JB094iB12p17907>, 1989.
- 1094 Novello, V.F., Cruz, F.W., Vuille, M., Strikis, N.M., Edwards, R.L., Cheng, H., Emerick, S., De Paula,  
1095 M.S., Li, X., Barreto, E.D.S., Karmann, I. A high-resolution history of the South American  
1096 Monsoon from Last Glacial Maximum to the Holocene. *Scientific Reports* 7(1), 44267,  
1097 <https://doi.org/10.1038/srep44267>, 2017.
- 1098 Orr, E.N., Owen, L.A., Saha, S., Caffee, M.W. Climate-driven late Quaternary fan surface abandonment  
1099 in the NW Himalaya. In: *Untangling the Quaternary Period—A Legacy of Stephen C. Porter*.  
1100 *Geological Society of America*, 63–80, [https://doi.org/10.1130/2020.2548\(04\)](https://doi.org/10.1130/2020.2548(04)), 2021.
- 1101 Owen, L.A., Clemmens, S.J., Finkel, R.C., Gray, H. Late Quaternary alluvial fans at the eastern end of  
1102 the San Bernardino Mountains, Southern California. *Quaternary Science Reviews*, 87, 114-  
1103 134. <https://doi.org/10.1016/j.quascirev.2014.01.003>, 2014.
- 1104 Paola, C., Heller, P.L., Angevine, C.L. The large-scale dynamics of grain-size variation in alluvial  
1105 basins, I: theory. *Basin Research*, 4, 73-90. [https://doi.org/10.1111/j.1365-  
1106 2117.1992.tb00145.x](https://doi.org/10.1111/j.1365-2117.1992.tb00145.x), 1992.
- 1107 Pedersen, V.K., Egholm, D.L. Glaciations in response to climate variations preconditioned by evolving  
1108 topography. *Nature*, 493(7431), 206-210. <https://doi.org/10.1038/nature11786>, 2013.
- 1109 Peri, V.G., Haghipour, N., Christl, M., Terrizzano, C., Kaveh-Firouz, A., Leiva, M.F., Pérez, P., Yamin,  
1110 M., Barcelona, H., Burg, J.P. Quaternary landscape evolution in the Western Argentine  
1111 Precordillera constrained by  $^{10}\text{Be}$  cosmogenic dating. *Geomorphology* 396,  
1112 <https://doi.org/10.1016/j.geomorph.2021.107984>, 2022.
- 1113 Perron, J.T., Royden, L. An integral approach to bedrock river profile analysis. *Earth Surface Processes*  
1114 *and Landforms*, 38(6), 570-576. <https://doi.org/10.1002/esp.3302>, 2013.
- 1115 Pingel, H., Strecker, M.R., Mulch, A., Alonso, R.N., Cottle, J., Rohrmann, A. Late Cenozoic  
1116 topographic evolution of the Eastern Cordillera and Puna Plateau margin in the southern Central  
1117 Andes (NW Argentina). *Earth and Planetary Science Letters* 535, 116112,  
1118 <https://doi.org/10.1016/j.epsl.2020.116112>, 2020.



- 1119 Pingel, H., Alonso, R.N., Altenberger, U., Cottle, J., Strecker, M.R. Miocene to Quaternary basin  
1120 evolution at the southeastern Andean Plateau (Puna) margin (ca. 24°S lat, Northwestern  
1121 Argentina). *Basin Research* 31, 808–826. <https://doi.org/10.1111/bre.12346>, 2019a.
- 1122 Pingel, H., Schildgen, T., Strecker, M.R., Wittmann, H. Pliocene–Pleistocene orographic control on  
1123 denudation in northwest Argentina. *Geology* 47, 359–362. <https://doi.org/10.1130/G45800.1>,  
1124 2019b.
- 1125 Pingel, H., Mulch, A., Alonso, R.N., Cottle, J., Hynek, S.A., Poletti, J., Rohrmann, A., Schmitt, A.K.,  
1126 Stockli, D.F. and Strecker, M.R. Surface uplift and convective rainfall along the southern  
1127 Central Andes (Angastaco Basin, NW Argentina). *Earth and Planetary Science Letters*, 440,  
1128 33–42. <https://doi.org/10.1016/j.epsl.2016.02.009>, 2016.
- 1129 Pingel, H., Strecker, M.R., Alonso, R.N., Schmitt, A.K. Neotectonic basin and landscape evolution in  
1130 the Eastern Cordillera of NW Argentina, Humahuaca Basin (~ 24 S). *Basin Research*, 25(5),  
1131 554–573. <https://doi.org/10.1111/bre.12016>, 2013.
- 1132 Placzek, C., Quade, J., Patchett, P.J. Geochronology and stratigraphy of late Pleistocene lake cycles on  
1133 the southern Bolivian Altiplano: implications for causes of tropical climate change. *Geological*  
1134 *Society of America Bulletin*, 118(5–6), 515–532. <https://doi.org/10.1130/B25770.1>, 2006.
- 1135 Prush, V.B., Oskin, M.E. A mechanistic erosion model for cosmogenic nuclide inheritance in single-  
1136 clast exposure ages. *Earth and Planetary Science Letters* 535, 116066.  
1137 <https://doi.org/10.1016/j.epsl.2020.116066>, 2020.
- 1138 Ratnayaka, K., Hetzel, R., Hornung, J., Hampel, A., Hinderer, M., Frechen, M. Postglacial alluvial fan  
1139 dynamics in the Cordillera Oriental, Peru, and palaeoclimatic implications. *Quaternary*  
1140 *Research*, 91, 431–449. <https://doi.org/10.1017/qua.2018.106>, 2019.
- 1141 Robinson, R.A.J., Spencer, J.Q.G., Strecker, M.R., Richter, A., Alonso, R.N. Luminescence dating of  
1142 alluvial fans in intramontane basins of NW Argentina. In: Harvey, A.M. et. al, eds. *Alluvial*  
1143 *Fans: Geomorphology, Sedimentology, Dynamics*. Geological Society. Special Publication  
1144 251, 153–168. 2005.
- 1145 Robledo Juan M., Luisa M. Anzótégui, Olga G. Martínez., Ricardo N. Alonso. Flora and insect trace  
1146 fossils from the Mio-Pliocene Quebrada del Toro locality (Gobernador Solá, Salta,  
1147 Argentina). *Journal of South American Earth Sciences*, Volume 100, June 2020, 102544.  
1148 <https://doi.org/10.1016/j.jsames.2020.102544>, 2020.
- 1149 Rohais, S., Bonnet, S. and Eschard, R. Sedimentary record of tectonic and climatic erosional  
1150 perturbations in an experimental coupled catchment-fan system. *Basin Research*, 24(2), 198–  
1151 212. <https://doi.org/10.1111/j.1365-2117.2011.00520.x>, 2012.
- 1152 Savi, S., Tofelde, S., Wickert, A.D., Bufe, A., Schildgen, T.F., Strecker, M.R. Interactions between  
1153 main channels and tributary alluvial fans: channel adjustments and sediment-signal  
1154 propagation. *Earth Surface Dynamics*, 8(2), 303–322. [https://doi.org/10.5194/esurf-8-303-  
1155 2020](https://doi.org/10.5194/esurf-8-303-2020), 2020.
- 1156 Savi, S., Schildgen, T.F., Tofelde, S., Wittmann, H., Scherler, D., Mey, J., Alonso, R.N., Strecker, M.R.  
1157 Climatic controls on debris-flow activity and sediment aggradation: The Del Medio fan, NW  
1158 Argentina. *Journal of Geophysical Research: Earth Surface* 121, 2424–2445.  
1159 <https://doi.org/10.1002/2016JF003912>, 2016.
- 1160 Schildgen, T.F., Robinson, R.A.J., Savi, S., Phillips, W.M., Spencer, J.Q.G., Bookhagen, B., Scherler,  
1161 D., Tofelde, S., Alonso, R.N., Kubik, P.W., Binnie, S.A., Strecker, M.R. Landscape response  
1162 to late Pleistocene climate change in NW Argentina: Sediment flux modulated by basin  
1163 geometry and connectivity. *Journal of Geophysical Research: Earth Surface* 121, 392–414.  
1164 <https://doi.org/10.1002/2015JF003607>, 2016.
- 1165 Schwab, K., Schäfer, A. Sedimentation und Tektonik im mittleren Abschnitt des Río Toro in der  
1166 Ostkordillere NW-Argentiniens. *Geologische Rundschau*, 65, 175–194.  
1167 <https://doi.org/10.1007/BF01808462>, 1976.
- 1168 Schwanghart, W., Scherler, D. Short Communication: TopoToolbox 2 – MATLAB-based software for  
1169 topographic analysis and modeling in Earth surface sciences. *Earth Surface Dynamics* 2, 1–7.  
1170 <https://doi.org/10.5194/esurf-2-1-2014>, 2014.
- 1171 Simpson, G., Castelltort, S. Model shows that rivers transmit high-frequency climate cycles to the  
1172 sedimentary record. *Geology* 40, 1131–1134. <https://doi.org/10.1130/G33451.1>, 2012.



- 1173 Seagren, E.G., Schoenbohm, L.M. Drainage reorganization across the Puna Plateau margin (NW  
1174 Argentina): Implications for the preservation of orogenic plateaus. *Journal of Geophysical*  
1175 *Research: Earth Surface*, 126(8), p.e2021JF006147. <https://doi.org/10.1029/2021JF006147>,  
1176 2021.
- 1177 Seagren, E.G., McMillan, M., Schoenbohm, L.M. Tectonic control on drainage evolution in broken  
1178 forelands: Examples from NW Argentina. *Tectonics*, 41(1), p.e2020TC006536,  
1179 <https://doi.org/10.1029/2020TC006536>, 2022.
- 1180 Spelz, R.M., Fletcher, J.M., Owen, L.A. and Caffee, M.W. Quaternary alluvial-fan development,  
1181 climate and morphologic dating of fault scarps in Laguna Salada, Baja California,  
1182 Mexico. *Geomorphology*, 102(3-4), 578-594.  
1183 <https://doi.org/10.1016/j.geomorph.2008.06.001>, 2008.
- 1184 Steffen, D., Schlunegger, F., Preusser, F. Late Pleistocene fans and terraces in the Majes valley,  
1185 southern Peru, and their relation to climatic variations. *International Journal of Earth*  
1186 *Sciences*, 99, 1975-1989. <https://doi.org/10.1007/s00531-009-0489-2>, 2010.
- 1187 Sternai, P., Herman, F., Valla, P.G., Champagnac, J.D. Spatial and temporal variations of glacial erosion  
1188 in the Rhône valley (Swiss Alps): Insights from numerical modeling. *Earth and Planetary*  
1189 *Science Letters* 368, 119–131. <https://doi.org/10.1016/j.epsl.2013.02.039>, 2013.
- 1190 Stone, J.O. Air pressure and cosmogenic isotope production. *Journal of Geophysical Research: Solid*  
1191 *Earth* 105, 23753–23759. 2000.
- 1192 Strecker, M.R., Alonso, R., Bookhagen, B., Carrapa, B., Coutand, I., Hain, M.P., Hilley, G.E.,  
1193 Mortimer, E., Schoenbohm, L., Sobel, E.R., 2009. Does the topographic distribution of the  
1194 central Andean Puna Plateau result from climatic or geodynamic processes? *Geology*, 37(7),  
1195 643-646. <https://doi.org/10.1130/G25545A.1>, 2009.
- 1196 Streit, R.L., Burbank, D.W., Strecker, M.R., Alonso, R.N., Cottle, J.M., Kylander-Clark, A.R.C.  
1197 Controls on intermontane basin filling, isolation and incision on the margin of the Puna Plateau,  
1198 NW Argentina (~23°S). *Basin Research* 29, 131–155. <https://doi.org/10.1111/bre.12141>, 2017.
- 1199 Terrizzano, C.M., García Morabito, E., Christl, M., Likerman, J., Tobal, J., Yamin, M., Zech, R.  
1200 Climatic and Tectonic forcing on alluvial fans in the Southern Central Andes. *Quaternary*  
1201 *Science Reviews* 172, 131–141. <https://doi.org/10.1016/j.quascirev.2017.08.002>, 2017.
- 1202 Tobal, J.E., Morabito, E.G., Terrizzano, C.M., Zech, R., Colavitto, B., Struck, J., Christl, M., Ghiglione,  
1203 M.C. Quaternary landscape evolution of Patagonia at the Chilean Triple Junction: Climate and  
1204 tectonic forcings. *Quaternary Science Reviews*, 261, 106960.  
1205 <https://doi.org/10.1016/j.quascirev.2021.106960>, 2021.
- 1206 Tofelde, S., Duesing, W., Schildgen, T.F., Wickert, A.D., Wittmann, H., Alonso, R.N., Strecker, M.  
1207 Effects of deep-seated versus shallow hillslope processes on cosmogenic <sup>10</sup>Be concentrations  
1208 in fluvial sand and gravel. *Earth Surface Processes and Landforms* 43, 3086–3098.  
1209 <https://doi.org/10.1002/esp.4471>, 2018.
- 1210 Tofelde, S., Savi, S., Wickert, A.D., Bufo, A., Schildgen, T.F. Alluvial channel response to  
1211 environmental perturbations: Fill-terrace formation and sediment-signal disruption. *Earth*  
1212 *Surface Dynamics* 7, 609–631. <https://doi.org/10.5194/esurf-7-609-2019>, 2019.
- 1213 Tofelde, S., Schildgen, T.F., Savi, S., Pingel, H., Wickert, A.D., Bookhagen, B., Wittmann, H., Alonso,  
1214 R.N., Cottle, J., Strecker, M.R. 100 kyr fluvial cut-and-fill terrace cycles since the Middle  
1215 Pleistocene in the southern Central Andes, NW Argentina. *Earth and Planetary Science Letters*  
1216 473, 141–153. <https://doi.org/10.1016/j.epsl.2017.06.001>, 2017.
- 1217 Uppala, S.M., Kållberg, P.W., Simmons, A.J., Andrae, U., Bechtold, V.D.C., Fiorino, M., Gibson, J.K.,  
1218 Haseler, J., Hernandez, A., Kelly, G.A., Li, X., Onogi, K., Saarinen, S., Sokka, N., Allan, R.P.,  
1219 Andersson, E., Arpe, K., Balmaseda, M.A., Beljaars, A.C.M., Berg, L. Van De, Bidlot, J.,  
1220 Bormann, N., Caires, S., Chevallier, F., Dethof, A., Dragosavac, M., Fisher, M., Fuentes, M.,  
1221 Hagemann, S., Hólm, E., Hoskins, B.J., Isaksen, L., Janssen, P.A.E.M., Jenne, R., McNally,  
1222 A.P., Mahfouf, J.-F., Morcrette, J.-J., Rayner, N.A., Saunders, R.W., Simon, P., Sterl, A.,  
1223 Trenberth, K.E., Untch, A., Vasiljevic, D., Viterbo, P., Woollen, J. The ERA-40 re-analysis.  
1224 *Quarterly Journal of the Royal Meteorological Society* 131, 2961–3012.  
1225 <https://doi.org/10.1256/qj.04.176>, 2005.



- 1226 Valla, P.G., Shuster, D.L., Van Der Beek, P.A. Significant increase in relief of the European Alps during  
1227 mid-Pleistocene glaciations. *Nature Geoscience*, 4(10), 688-692.  
1228 <https://doi.org/10.1038/ngeo1242>, 2011.
- 1229 van den Berg, van Saparoea, A.-P. H., Postma, G. Control of climate change on the yield of river  
1230 systems, Recent Adv. Model. Siliciclastic Shallow-Marine Stratigr. SEPM Spec. Publ., 90, 15–  
1231 33, 2008, <https://doi.org/10.2110/pec.08.90.0015>
- 1232 Ventra, D., Nichols, G.J. Autogenic dynamics of alluvial fans in endorheic basins: outcrop examples  
1233 and stratigraphic significance. *Sedimentology*, 61(3), 767-791.  
1234 <https://doi.org/10.1111/sed.12077>, 2014.
- 1235 Vera, C., Higgins, W., Amador, J., Ambrizzi, T., Garreaud, R., Gochis, D., Gutzler, D., Lettenmaier,  
1236 D., Marengo, J., Mechoso, C.R., Noguez-Paegle, J. Toward a unified view of the American  
1237 monsoon systems. *Journal of Climate*, 19(20), 4977-5000. <https://doi.org/10.1175/JCLI3896.1>,  
1238 2006.
- 1239 Vezzoli, L., Acocella, V., Omarini, R., Mazzuoli, R. Miocene sedimentation, volcanism and  
1240 deformation in the Eastern Cordillera (24°30' S, NW Argentina): Tracking the evolution of the  
1241 foreland basin of the Central Andes. *Basin Research* 24, 637–663.  
1242 <https://doi.org/10.1111/j.1365-2117.2012.00547.x>, 2012.
- 1243 Vizu, E.K., Cook, K.H. Relationship between Amazon and high Andes rainfall. *Journal of Geophysical*  
1244 *Research: Atmospheres*, 112(D7). <https://doi.org/10.1029/2006JD007980>, 2007.
- 1245 von Blanckenburg, F. Cosmogenic nuclide evidence for low weathering and denudation in the wet,  
1246 tropical highlands of Sri Lanka. *Journal of Geophysical Research: Earth Surface*, 109, F03008.  
1247 <https://doi.org/10.1029/2003JF000049>, 2004.
- 1248 Wang, X., Auler, A.S., Edwards, R.L., Cheng, H., Ito, E., Wang, Y., Kong, X., Solheid, M. Millennial-  
1249 scale precipitation changes in southern Brazil over the past 90,000 years. *Geophysical Research*  
1250 *Letters* 34 (23). <https://doi.org/10.1029/2007GL031149>, 2007.
- 1251 Wickert, A.D., Schildgen, T.F. Long-profile evolution of transport-limited gravel-bed rivers. *Earth*  
1252 *Surface Dynamics*, 7(1), 17-43. <https://doi.org/10.5194/esurf-7-17-2019>, 2019.
- 1253 Wittmann, H., Malusà, M.G., Resentini, A., Garzanti, E., Niedermann, S. The cosmogenic record of  
1254 mountain erosion transmitted across a foreland basin: Source-to-sink analysis of in situ <sup>10</sup>Be,  
1255 <sup>26</sup>Al and <sup>21</sup>Ne in sediment of the Po river catchment. *Earth and Planetary Science Letters* 452,  
1256 258–271. <https://doi.org/10.1016/j.epsl.2016.07.017>, 2016.
- 1257 Zech, J., Terrizzano, C.M., Garcia Morabito, E., Veit, H., Zech, R. Timing and extent of late Pleistocene  
1258 glaciation in the arid Central Andes of Argentina and Chile (22°-41°S). *CIG* 43(2):697-  
1259 718. <http://dx.doi.org/10.18172/cig.3235>, 2017.
- 1260 Zondervan, J.R., Stokes, M., Boulton, S.J., Telfer, M.W., Mather, A.E. Rock strength and structural  
1261 controls on fluvial erodibility: Implications for drainage divide mobility in a collisional  
1262 mountain belt. *Earth and Planetary Science Letters*, 538, 116221.  
1263 <https://doi.org/10.1016/j.epsl.2020.116221>, 2020.  
1264